





Interorbital Cooper pairing at finite energies in Rashba surface states

Philipp Rüßmann ^{1,2,*}, Masoud Bahari ^{1,3,†}, Stefan Blügel ², and Björn Trauzettel ^{1,3}

¹*Institute for Theoretical Physics and Astrophysics, University of Würzburg, D-97074 Würzburg, Germany*

²*Peter Grünberg Institut and Institute for Advanced Simulation, Forschungszentrum Jülich and JARA, D-52425 Jülich, Germany*

³*Würzburg-Dresden Cluster of Excellence ct.qmat, Germany*



(Received 26 July 2023; revised 23 October 2023; accepted 25 October 2023; published 27 November 2023)

Multiband effects in hybrid structures provide a rich playground for unconventional superconductivity. We combine two complementary approaches based on density-functional theory (DFT) and effective low-energy model theory in order to investigate the proximity effect in a Rashba surface state in contact with an s -wave superconductor. We discuss these synergistic approaches and combine the effective model and DFT analysis at the example of a Au/Al heterostructure. This allows us to predict finite-energy superconducting pairing due to the interplay of the Rashba surface state of Au, and hybridization with the electronic structure of superconducting Al. We investigate the nature of the induced superconducting pairing, and we quantify its mixed singlet-triplet character. Our findings demonstrate general recipes to explore real material systems that exhibit interorbital pairing away from the Fermi energy.

DOI: [10.1103/PhysRevResearch.5.043181](https://doi.org/10.1103/PhysRevResearch.5.043181)

I. INTRODUCTION

Materials that exhibit strong spin-orbit coupling (SOC) build the foundation for a plethora of physical phenomena [1,2] with various applications in noncollinear topological magnetic textures (e.g., skyrmions) [3], spinorbitronics [1] or topological insulators [4], and quantum-information processing [5–8]. Combining different materials in heterostructures not only gives rise to breaking of symmetries, which is essential to Rashba SOC [9], but it also allows us to tailor proximity effects, where the emergent physics of the heterostructure as a whole is richer than the sum of its constituents. In the past, this has attracted a lot of interest in the context of increasing SOC in graphene [10–12]. Combining a strong-SOC material with a superconductor is, moreover, of particular use to realize topological superconductivity, which can host Majorana zero modes (MZMs). In turn, MZMs are building blocks of topological qubits [13]. For instance, signatures of MZMs have been recently been observed in V/Au/EuS heterostructures both in experiment [14] as well as in theory [15].

In this work, we study the interorbital physics inherent to heterostructures consisting of superconductors and Rashba materials. We combine theoretical modeling of two complementary approaches that have their roots in rather disjoint communities focusing on either microscopic or mesoscopic physics. We combine the predictive power of material-specific

DFT simulations with the physical insights of an analytically solvable low-energy model. The Bogoliubov–de Gennes (BdG) formalism [16,17] is the basis for both models, in particular the DFT-based description of the superconducting state, commonly referred to as the Kohn-Sham Bogoliubov–de Gennes (KS-BdG) approach [18–22]. While DFT naturally accounts for multiband effects, the effective low-energy model with a simpler treatment of only a few bands allows us to identify the symmetry of the superconducting pairing. Crystal symmetries have profound effects. For example, they may or may not cause wave functions to overlap, which is visible in DFT calculations. A group-theoretic analysis allows us to infer possible (unconventional) pairing channels from crystal symmetries [23]. However, group theory alone does not tell us which of the possible pairing channels really matters in a given material. Hence, only the combination of both approaches (DFT and group theory) is able to predict the emergence of experimentally relevant (unconventional) pairing channels in the laboratory.

Rashba SOC is intimately related to orbital mixing, often involving p electrons [2]. Evidence for strong Rashba-SOC is found in a variety of materials such as heavy metal surfaces (e.g., Au or Ir) and surface alloys (e.g., $\sqrt{3} \times \sqrt{3}$ Bi/Ag) [24–26], semiconductors (e.g., InSb) [27], and topological insulators (e.g., Bi₂Se₃) [28]. We investigate the combination of such metals in hybrid structures with common superconductors, where multiband effects are essential. In general, multiband effects have crucial implications. They are, for instance, relevant for transport across superconductor-semiconductor interfaces in the presence of Fermi surface mismatch [29], and they play a major role in the superconducting diode effect [30–32]. Recently, the possibility to observe finite-energy pairing has emerged as an additional tool to study the nature of unconventional pairing [33–36], where, furthermore, topological phase transitions have been

*philipp.rueßmann@uni-wuerzburg.de

†masoud.bahari@physik.uni-wuerzburg.de

Published by the American Physical Society under the terms of the [Creative Commons Attribution 4.0 International](https://creativecommons.org/licenses/by/4.0/) license. Further distribution of this work must maintain attribution to the author(s) and the published article's title, journal citation, and DOI.

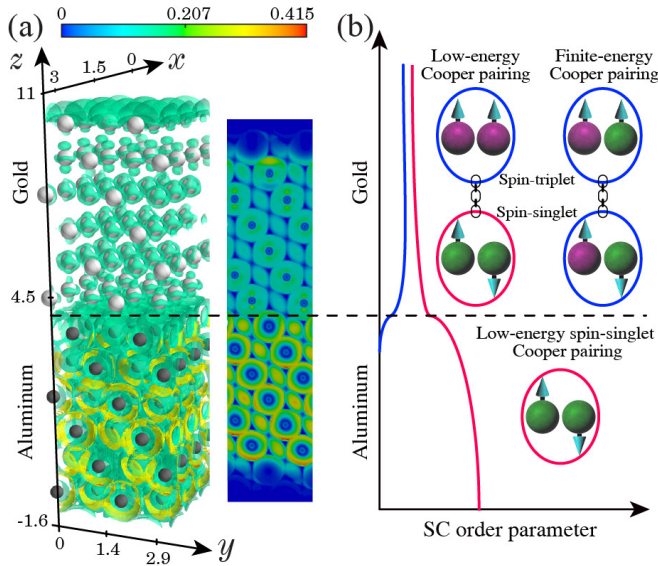


FIG. 1. (a) Localization of the electron density (arb. units) around the Fermi energy throughout the Al/Au heterostructure. The background shows a cut through $x = 0$. (b) Illustration of three kinds of Cooper pair tunneling and the formation of different singlet/triplet components due to the Rashba surface state. Cooper pairs formed by electrons originating from different orbitals are denoted by different colors.

predicted [37]. This is a direct consequence of the rich physics of unconventional Cooper pairing that is possible in multiband superconductors [33–41].

As a prime example experiencing the multiband physics of a proximitized Rashba state, we identify the interface between aluminum (Al) and gold (Au). This combination allows us to study the proximity effect with Rashba surface states. On the one hand, Al is a well-known and widely used s -wave superconductor whose valence-band electrons are of s - p orbital character. On the other hand, Au is a simple heavy metal in which the effects of strong SOC are particularly pronounced. In fact, as a consequence of strong SOC, the (111) surface of Au hosts a set of two spin-momentum-locked Rashba surface states [24,42–46]. Both Al and Au grow in the face-centered-crystal (fcc) structure, and their lattice constants vary only marginally [47,48]. Hence, epitaxial growth of this heterostructure is feasible. It is ideally suited to gain insight into (i) hybridization of the electronic structure of Al- and Au-derived bands at the interface, (ii) the proximity effect of the SOC from Au into the superconductor Al, (iii) the interplay of the superconducting proximity effect and SOC in this multiband system, and (iv) the mixed singlet-triplet nature of induced superconducting pairing. The hybridized electronic structure in the Al/Au heterostructure and the emerging superconducting pairing channels due to multiband effects are depicted in Fig. 1.

This article is structured as follows. In Sec. II, the normal state electronic structure of the Au/Al heterostructure is discussed with DFT and low-energy model approaches. In Sec. III, the DFT and model access to superconducting heterostructures are presented with emphasis on complementary insights. This modeling allows us to study the proximity

effects of SOC and superconductivity in multiband systems at the example of Al/Au interfaces. We conclude in Sec. IV, where we also comment on the feasibility of experimental detection of our predictions.

II. NORMAL STATE SPECTRUM

The DFT and model-based approaches described in this article are complementary and uniquely distinct in their methodologies. The DFT-based numerical calculations provide an *ab initio* approach to the description of the electronic structure of the normal state, and their scope encompasses *all* electronic degrees of freedom, resulting in a precise and extensive representation applicable to a broad range of materials merely from the knowledge about the crystal structure. Consequently, the intricate band structure generated by this method can be complex, comprising several bands with diverse orbital and spin character.

The effective low-energy model aims to simplify the complexity of the electronic structure by describing only a few bands, particularly those close to the Γ -point and the Fermi level. The model-based approach has the distinct advantage of deriving analytical expressions that can be applied to a wide range of material classes. Additionally, the model enables the analysis and inclusion of certain symmetries. For instance, only odd terms in \mathbf{k} might appear in certain parts of the model Hamiltonian. To create a model that applies to a real material, however, it is necessary to determine model parameters by fitting to experimental or DFT data.

A. Density-functional-theory results

Our DFT calculations for heterostructures, consisting of thin Al and Au films, are summarized in Figs. 1 and 2(a)–2(d). Both Al and Au have a face-centered-cubic (fcc) crystal structure with lattice constants of 4.08 Å and 4.05 Å, respectively [47,48]. We investigate an ideal interface in the close-packed (111) surface of the fcc lattice. To model the heterostructure, we use a unit cell that consists of six layers of Al and six layers of Au with the average experimental lattice constant of Al and Au, differing only by about 0.4% from their respective bulk lattice constants. For our DFT calculations, we employ the full-potential relativistic Korringa-Kohn-Rostoker Green function method, as implemented in the JuKKR code [49]. This allows us to include the effect of superconductivity on the footings of the Bogoliubov–de Gennes formalism [50]. Computational details are provided in Appendix A.

The electronic structure of Au below the Fermi level is dominated by the fully occupied shell of d -electrons around -2 to -8 eV (see Appendix B for the corresponding DOS). In thin-film heterostructures (called “slabs”), the electrons are confined inside the slab, leading to finite-size quantization and the appearance of two-dimensional quantum-well states manifested as a series of discrete bands in the region where the bulk electronic structure is projected into the surface Brillouin zone. The presence of surfaces and interfaces, and the possible appearance of broken bonds, often leads to additional surface states or surface resonances in the electronic structure. For the Au(111) surface, Rashba surface states appear in surface

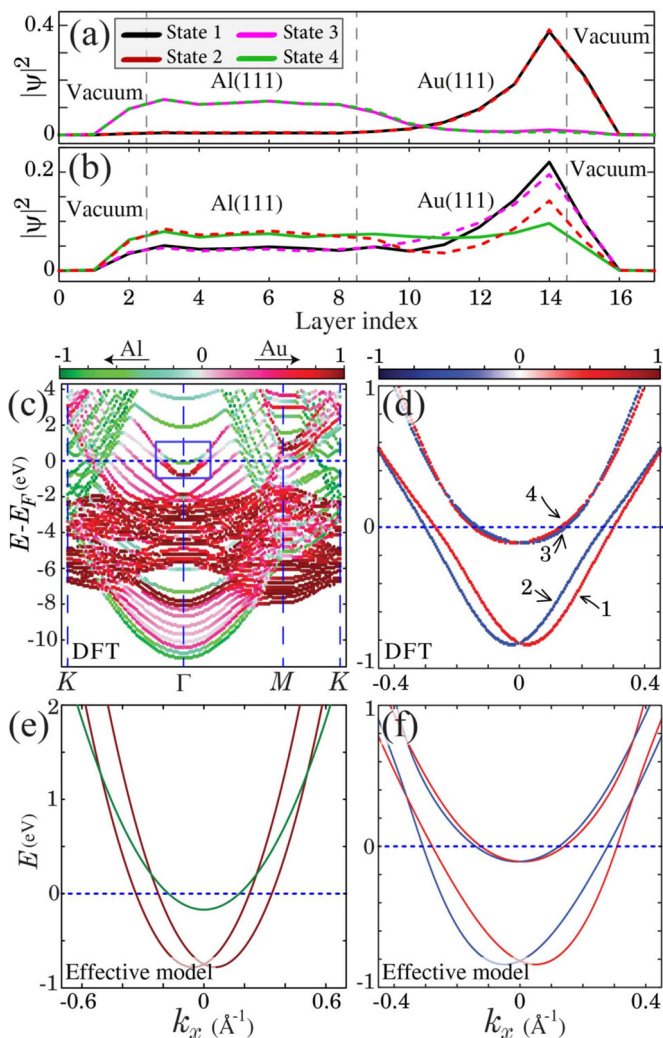


FIG. 2. DFT wave-function localization in the Al/Au hybrid structure consisting of six layers of each element at the two k -points (a) $k_x = 0.1 \text{ \AA}^{-1}$ and (b) $k_x = 0.3 \text{ \AA}^{-1}$ for the four states labeled in panel (d). (c) Corresponding large-scale DFT band structure. The color bar shows the localization of the states. (d) Enlarged view of the spectrum close to the Fermi energy denoted by the blue rectangle in panel (e). The color bar shows the spin polarization (s_y) (arb. units). (e) [(f)] Excitation spectrum of the normal state obtained by the low-energy model Hamiltonian, given in Eq. (1), close to the Fermi energy in the absence (presence) of band hybridization and including third-order Rashba spin-orbit coupling, i.e., $F_0 = g = 0$ ($F_0 = 0.2$ and $g = -8.45$). Other model parameters are given in Table I.

projection of the bulk L -gap around the Γ point of the surface Brillouin zone. They are of s - p_z orbital character [24,43].

The region around Γ , highlighted by the blue box in Fig. 2(c), is the focus of our study. It is enlarged in Fig. 2(d). The in-plane component of the spin-polarization (s_y) perpendicular to the direction of the momentum (k_x) is shown by the color coding of the bands. Note that, due to crystal symmetries, s_x is exactly zero in the plane through $k_y = 0$, and s_z is negligibly small. From the full band-structure information based on DFT, we select a regime of interest for the analytical effective low-energy model. We restrict our analysis to the four states labeled 1–4, which (at small $|\mathbf{k}|$ close to

Γ) are derived from the Rashba surface state of Au (states 1,2) or Al (states 3,4), respectively. The Al states (3,4) have a quadratic dispersion and show much weaker spin-splitting. Importantly, our study reveals the existence of only a single pair of Au Rashba surface states localized at the interface of Au and vacuum. Notably, no second pair of states arises from the interface of Al and Au. This can be deduced from the localization of these states depicted in Figs. 2(a) and 2(b). The wave-function localization is shown for two values of the momentum: close to Γ at $k_x = 0.1 \text{ \AA}^{-1}$ [panel (a)] where the Al- and Au-derived states are clearly distinct, and at larger momentum of $k_x = 0.3 \text{ \AA}^{-1}$ [panel (b)] where the four bands clearly interact. At smaller momentum, the Rashba surface states (1,2) are exponentially localized at the Au-vacuum interface and have a negligible overlap with the states 3 and 4, which are delocalized throughout the Al film. In contrast, at larger momenta the four states hybridize, which can be seen in the significant weight of all states in both the layers of Al and Au. This is particularly visible in comparing the panels (a,b) of Fig. 2 around layer 5 (in Al) and layer 14 (i.e., the Au surface). The real-space distribution of the charge density at the Fermi energy is shown in Fig. 1(a). We conclude that the scattering potential at the interface is weak enough to prevent the formation of a second state at the Al/Au interface.

Aluminum is a light metal with negligible intrinsic SOC. The small SOC-induced spin-splitting seen for states 3,4 is merely a result of a proximity-induced SOC from Au to Al, hinting at sizable hybridization of the electronic structure of Al and Au. In Sec. II B, we discuss in detail that, at higher momenta, the parabolas of the Al-derived states and the Rashba surface states intersect and hybridize, resulting in more delocalized states throughout the entire Al-Au heterostructure. This hybridization can be attributed to the compatible orbital character of the Al and Au bands, which both possess s - p_z -like orbital character. Ultimately, this hybridization leads to the proximity effect of the spin-orbit coupling (SOC) observed in the Al quantum-well states.

B. Effective low-energy model

Complementary to our DFT results, we develop an effective four-band model Hamiltonian to evaluate the spectral properties of the heterostructure in an analytical manner. Guided by the insights from our DFT calculation, we construct a model for the proximitized Rashba surface state. We note a hybridization of spin-split Au surface bands and the doubly degenerate Al band near the Fermi energy. Thus, we propose the normal state model Hamiltonian to be

$$H_N = \sum_{\mathbf{k}} (c_{\mathbf{k},\text{Al}}^\dagger, c_{\mathbf{k},\text{Au}}^\dagger) \begin{pmatrix} \hat{h}_{\text{Al}}(\mathbf{k}) & F_0 \hat{\sigma}_0 \\ F_0 \hat{\sigma}_0 & \hat{h}_{\text{Au}}(\mathbf{k}) \end{pmatrix} \begin{pmatrix} c_{\mathbf{k},\text{Al}} \\ c_{\mathbf{k},\text{Au}} \end{pmatrix}, \quad (1)$$

where the electron annihilation operator is denoted as $c_{\mathbf{k},\nu} = (c_{\mathbf{k},\nu,s}, c_{\mathbf{k},\nu,-s})^T$ labeled by the 2D momentum vector $\mathbf{k} = (k_x, k_y)$ with orbital ($\nu \in \{\text{Al}, \text{Au}\}$) and spin ($s \in \{\uparrow, \downarrow\}$) degrees of freedom. F_0 signifies the hybridization strength between Al and Au bands. Furthermore, $\hat{h}_{\text{Al(Au)}}(\mathbf{k})$ denotes

TABLE I. Values for the parameters of the low-energy model given in Eq. (4).

	α_i (eV Å ²)	μ_i (eV)	F_0 (eV)	λ (eV Å)	g (eV Å ³)
Al	5.6	0.17	0.2	1.1	-8.45
Au	10	0.75			

the 2×2 sector for the Al (Au) segment given by

$$\hat{h}_{\text{Al}}(\mathbf{k}) = (\alpha_{\text{Al}}k^2 - \mu_{\text{Al}})\hat{\sigma}_0, \quad (2)$$

$$\begin{aligned} \hat{h}_{\text{Au}}(\mathbf{k}) &= (\alpha_{\text{Au}}k^2 - \mu_{\text{Au}})\hat{\sigma}_0 + \lambda(\hat{\sigma}_x k_y - k_x \hat{\sigma}_y) \\ &+ g[\hat{\sigma}_x(k_y^3 + k_y k_x^2) - (k_x^3 + k_x k_y^2)\hat{\sigma}_y], \end{aligned} \quad (3)$$

where $k \equiv |\mathbf{k}| = \sqrt{k_x^2 + k_y^2}$; $\alpha_{\text{Al(Au)}}$ and $\mu_{\text{Al(Au)}}$ characterize the mass term and chemical potential for Al (Au) bands, respectively. First-order (third-order) spin-orbit coupling in the Au sector is parametrized by λ (g) leading to broken inversion symmetry, i.e., $\hat{h}_{\text{Au}}(-\mathbf{k}) \neq \hat{h}_{\text{Au}}(\mathbf{k})$. It is worth noting that even though the band spin-splitting of the Rashba surface state is isotropic in Au [24], it is necessary to consider higher-order polynomials for the Rashba SOC in the heterostructure to match the dispersion calculated from first-principles. We attribute this observation to the reduced C_{3v} point group symmetry of the interface built into the DFT model via the chosen crystal structure. We obtain the third-order polynomial presented in the last term of Eq. (3) by taking the direct product of the irreducible representations of C_{3v} [51]. Hence, this normal-state model is constructed by intuition employing the $\mathbf{k} \cdot \mathbf{p}$ approach. This is evident in our formulation of the Hamiltonian, where we combine a Rashba model up to third order describing the Au layer with a quadratic dispersion for the Al layer and a band hybridization term F_0 .

For simplicity, we focus on the 1D Brillouin zone, i.e., $\mathbf{k} = (k_x, 0)$, since our model is rotationally symmetric. Therefore, the excitation spectra of the hybrid structure become

$$E_{\mathbf{k},s}^{s'} = \frac{1}{2}(\mathcal{E}_{\text{Al}} + \mathcal{E}_{\text{Au}}^s + s' \sqrt{(\mathcal{E}_{\text{Al}} - \mathcal{E}_{\text{Au}}^s)^2 + 4F_0^2}), \quad (4)$$

where $s, s' \in \{+, -\}$. The quadratic band in the Al segment is denoted as $\mathcal{E}_{\text{Al}} = \alpha_{\text{Al}}k^2 - \mu_{\text{Al}}$, and the spin-split band in the Au segment is denoted as $\mathcal{E}_{\text{Au}}^{\pm} = \alpha_{\text{Au}}k^2 \pm (k\lambda + gk^3) - \mu_{\text{Au}}$ [Fig. 2(e)]. Due to hybridization, an effective spin-orbit coupling is induced in the doubly degenerate Al bands, ultimately leading to the lifting of their degeneracy. After fitting to the DFT data, the analytical spectra given by Eq. (4) are in excellent agreement with the DFT calculation; compare Figs. 2(d) and 2(f) where the model fitted model parameters are summarized in Table I.

III. SUPERCONDUCTING EXCITATION SPECTRUM

In general, a microscopic theoretical description of the superconducting excitations can be achieved on the basis of the Bogoliubov–de Gennes (BdG) formalism [16,17], a generalization of the BCS theory of superconductivity [52]. The BdG formalism is based on the Hamiltonian

$$\hat{\mathcal{H}}_{\text{BdG}} = \begin{pmatrix} \hat{H}_0 & \hat{\Delta} \\ [\hat{\Delta}]^\dagger & -\hat{H}_0^* \end{pmatrix}, \quad (5)$$

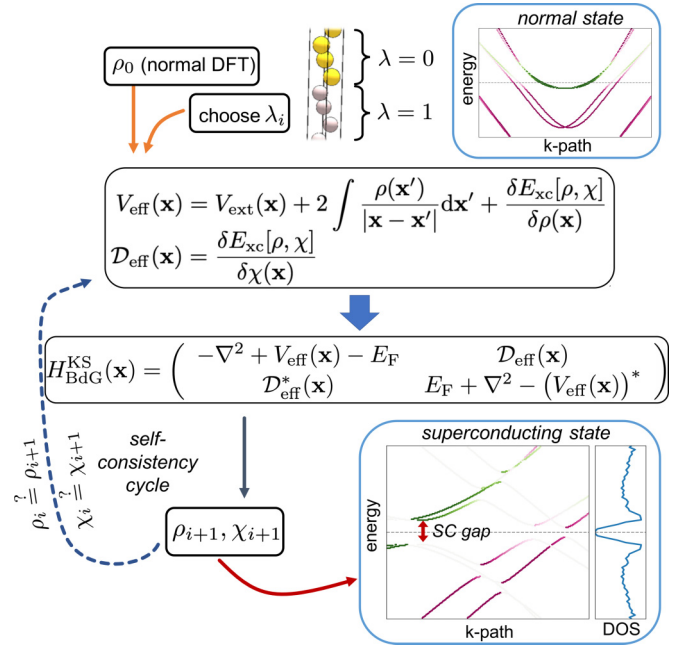


FIG. 3. Schematic overview of a KS-BdG simulation that starts from the crystal structure which (in a standard DFT calculation) gives the ground-state density ρ_0 . For the superconducting state, the KS-BdG equations are then solved self-consistently to obtain charge and anomalous densities ρ, χ in the superconducting state, which determines the superconducting band structure.

where \hat{H}_0 denotes the normal state Hamiltonian and $\hat{\Delta}$ is the superconducting pairing between particle and hole blocks. The BdG method is also key to the extension of DFT for superconductors [18–22], commonly referred to as the Kohn-Sham Bogoliubov–de Gennes (KS-BdG) formalism. One major difference between DFT and model formulations is that Eq. (5) is formulated in real space (DFT) or momentum space (model) if translation invariance is given.

A. Kohn-Sham Bogoliubov–de Gennes formalism

The central task in the superconducting DFT approach (sketched in Fig. 3) is to solve the Kohn-Sham BdG (KS-BdG) equation [18,20,53]

$$H_{\text{BdG}}^{\text{KS}}(\mathbf{x})\Psi_v^{\text{KS}}(\mathbf{x}) = \varepsilon_v \Psi_v^{\text{KS}}(\mathbf{x}), \quad (6)$$

which is a reformulation of the Schrödinger equation (or the Dirac equation if relativistic effects are taken into account) in terms of an effective single-particle picture. The effective single-particle wave functions in Nambu space, $\Psi_v^{\text{KS}}(\mathbf{x}) = (u_v(\mathbf{x}), v_v(\mathbf{x}))^T$, describe, respectively, the particle and hole components at excitation energy ε_v (v is a band index labeling the electronic degrees of freedom). The KS-BdG Hamiltonian can be written in matrix form as [20,50]

$$H_{\text{BdG}}^{\text{KS}}(\mathbf{x}) = \begin{pmatrix} H_0^{\text{KS}}(\mathbf{x}) - E_F & \Delta_{\text{eff}}(\mathbf{x}) \\ \Delta_{\text{eff}}^*(\mathbf{x}) & E_F - (H_0^{\text{KS}}(\mathbf{x}))^* \end{pmatrix}, \quad (7)$$

where E_F is the Fermi energy. The normal state Hamiltonian

$$H_0^{\text{KS}}(\mathbf{x}) = -\nabla^2 + V_{\text{eff}}(\mathbf{x}) \quad (8)$$

and the effective superconducting pairing potential Δ_{eff} appear in the Kohn-Sham formulation (Rydberg atomic units are used where $\hbar = 1$). For $\Delta_{\text{eff}} = 0$, the KS-BdG equation reduces to solving the conventional Kohn-Sham equation of DFT that describes the electronic structure of the normal state.

The effective single-particle potentials in Eq. (7) are functionals of the charge density $\rho(\mathbf{x})$ and the anomalous density $\chi(\mathbf{x})$ (the superconducting order parameter) [18,53],

$$V_{\text{eff}}(\mathbf{x}) = V_{\text{ext}}(\mathbf{x}) + 2 \int \frac{\rho(\mathbf{x}')}{|\mathbf{x} - \mathbf{x}'|} d\mathbf{x}' + \frac{\delta E_{\text{xc}}[\rho, \chi]}{\delta \rho(\mathbf{x})}, \quad (9)$$

$$\Delta_{\text{eff}}(\mathbf{x}) = \frac{\delta E_{\text{xc}}[\rho, \chi]}{\delta \chi(\mathbf{x})}, \quad (10)$$

where functional derivatives of the exchange correlation functional E_{xc} appear requiring a self-consistent solution of the nonlinear KS-BdG equations. The exchange correlation functional can be expressed as [53]

$$E_{\text{xc}}[\rho, \chi] = E_{\text{xc}}^0[\rho] - \int \chi^*(\mathbf{x}) \lambda \chi(\mathbf{x}) d\mathbf{x}, \quad (11)$$

where the conventional exchange-correlation functional E_{xc}^0 is the standard DFT term (in the normal state).

It is important to note that the above formulation of the KS-BdG equations assumes a simplified form of the superconducting pairing kernel [53] [i.e., the second term in Eq. (11)], which reduces λ to simple constants within the cells surrounding the atoms that are nevertheless allowed to take different values throughout the computational unit cell. This assumes that the pairing interaction is local in space. This approximation was successfully used to study conventional s -wave superconductors [20,50,54,55], heterostructures of s -wave superconductors and nonsuperconductors [56–58], or impurities embedded into superconductors [59,60]. Hence, the effective pairing interaction takes the simple form [53]

$$\Delta_{\text{eff}}(\mathbf{x}) = \lambda_i \chi(\mathbf{x}), \quad (12)$$

where λ_i is a set of effective coupling constants describing the intrinsic superconducting coupling that is allowed to depend on the position i in the unit cell.

Finally, the charge density ρ and the anomalous density χ are calculated from the particle (u_ν) and hole components (v_ν) of the wave function,

$$\rho(\mathbf{x}) = 2 \sum_\nu f(\varepsilon_\nu) |u_\nu(\mathbf{x})|^2 + [1 - f(\varepsilon_\nu)] |v_\nu(\mathbf{x})|^2, \quad (13)$$

$$\chi(\mathbf{x}) = \sum_\nu [1 - 2f(\varepsilon_\nu)] u_\nu(\mathbf{x}) v_\nu^*(\mathbf{x}), \quad (14)$$

where $f(\varepsilon)$ is the Fermi-Dirac distribution function, and the summation over ν includes the full spectrum of the KS-BdG Hamiltonian.

B. DFT results for superconducting Al/Au

For the superconducting state, we assume that only Al has an intrinsic superconducting coupling, and we set the layer-dependent coupling constant in the KS-BdG calculation to

$$\lambda_i = \begin{cases} \lambda_{\text{Al}} & \text{if } i \in \text{Al}, \\ 0 & \text{otherwise,} \end{cases} \quad (15)$$

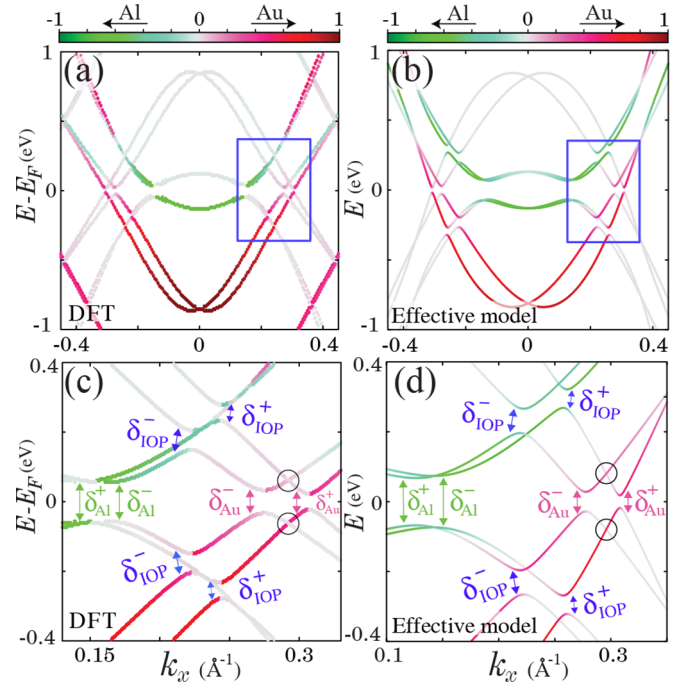


FIG. 4. Superconducting band structure of the Al/Au heterostructure obtained by (a) DFT and (b) the low-energy model. The red/green and gray bands indicate the particle and hole character of the BdG bands, respectively. The red/green color of the particle bands indicates the localization of the states. Panels (c) and (d) show an enlarged view of the region marked by the blue box in (a) where six different superconducting avoided crossings emerge (labeled δ_{Al}^{\pm} , δ_{Au}^{\pm} , and $\delta_{\text{IOP}}^{\pm}$). The absence of avoided crossings marked by black circles in (c) and (d) is due to pseudo-spin-rotational symmetry. For illustration purposes, we show results for scaled-up values of the superconducting pairing. The model parameters for the analytical model are those given in Table I and $\Delta = 0.4F_0$.

where λ_{Al} is a positive real-valued constant and i is an index counting the atomic layers in the Al/Au heterostructure. While the value of λ_{Al} can be regarded as a fitting parameter in this approach, we stress that only an integral quantity, leading to the overall superconducting gap size in thin films of Al, is fitted. Other spectral properties such as avoided crossings and proximity effects are in fact predictions of this theory. The results of our KS-BdG simulations and analytical model for the Al/Au heterostructure are summarized in Fig. 4. For better visibility, we show results for scaled-up values of the superconducting pairing (i.e., larger values for λ_{Al}). The general trends we discuss here are, however, transferable from large to small pairing strengths with only quantitative changes. We find superconducting gaps and avoided crossings at low and finite excitation energies, labeled with δ in Fig. 4(c). These avoided crossings are rooted in the s -wave superconductivity induced from the Al segment included in the DFT-based simulations by λ_i (the *only* adjustable parameter in our description of the superconducting state). The hybridization between Al and Au bands enables Cooper pair tunneling from the superconductor into the metal [see Fig. 1(b)]. This results in a superconducting proximity effect in the Rashba surface state of Au. The large spin-splitting of the Rashba surface state

allows for the pairing to have triplet character because the superconducting hybridization happens between quasiparticle bands with identical pseudospin degrees of freedom. This will be further explained in the effective model analysis of Sec. III C.

The DFT calculations disclose the anisotropy of the pairing gap (see Fig. 4), which is stronger for the Rashba state at smaller momentum with $\delta_{\text{Au}}^- \approx 0.51\delta_{\text{Al}}^\pm$ and decreases to $\delta_{\text{Au}}^+ \approx 0.38\delta_{\text{Al}}^\pm$ for the state at larger momentum. Furthermore, we also observe that interorbital pairings appear away from the Fermi energy, as indicated by δ_{IOP}^\pm , where the states with dominant Au orbital character and pseudo-spin-up intersects with the hole states with dominant Al orbital character having pseudo-spin-down degrees of freedom. This phenomenon has been referred to as interband pairing [33,34,38–40], mirage gap [35], and finite-energy Cooper pairing [36,37,41]. However, conclusive experimental evidence supporting it is still elusive. The Al/Au hybrid structure presented here provides a simple system in which such finite-energy pairing can be observed.

Similar to the two pairing gaps δ_{Au}^\pm in the Rashba surface state, the DFT calculation shows that the interorbital pairings δ_{IOP} also decrease at larger momentum, i.e., $\delta_{\text{IOP}}^-/\delta_{\text{Al}} = 0.60$ to $\delta_{\text{IOP}2}^+/\delta_{\text{Al}} = 0.44$. Based on these observations, we pose four questions:

(Q.1) Is interorbital pairing exclusively the result of superconducting order or other mechanisms?

(Q.2) What determines the magnitude of the finite-energy pairing?

(Q.3) What is the magnitude of the induced spin-singlet and triplet components of the effective pairing?

(Q.4) What specific symmetries are responsible for protecting certain electron-hole band crossings that occur away from the Fermi energy?

These questions will be answered in the following sections.

C. Effective low-energy model for the superconducting heterostructure

Based on an effective low-energy model, we can achieve a deeper understanding of the KS-BdG results. The results of our low-energy model are illustrated in Figs. 4(b) and 4(d). They are obtained by the model introduced in Sec. II B. To obtain an analytical characterization of the superconducting pairing in the heterostructure, it is necessary to construct a BdG formalism for our minimal model, cf. Eq. (1). Assuming that the superconducting pairing arises from the Al layer, we model the single-particle pairing operator as

$$H_\Delta = \sum_{\mathbf{k}} (c_{\mathbf{k},\text{Al}}^\dagger, c_{\mathbf{k},\text{Au}}^\dagger) \begin{pmatrix} \Delta i\hat{\sigma}_y & 0 \\ 0 & 0 \end{pmatrix} \begin{pmatrix} c_{-\mathbf{k},\text{Al}}^\dagger \\ c_{-\mathbf{k},\text{Au}}^\dagger \end{pmatrix}, \quad (16)$$

where Δ denotes the superconducting pairing strength, and the nonvanishing diagonal entry corresponds to *s*-wave spin singlet pairing in the Al layer. Since pure Au does not become a superconductor at experimentally relevant temperatures, the pairing strength in the Au layer is set to zero. Note that the momentum-space formulation in the model approach directly relates to the real-space formulation used in the DFT approach. This is evident since in Eq. (16) intrinsic supercon-

ducting pairing is only added within the Al bands, while in the DFT approach Δ_{eff} [cf. Eqs. (7) and (10)] is only nonzero within the Al atoms.

It is illuminating to represent the BdG Hamiltonian in the eigenbasis of the normal state, given in Eq. (1), as defined by the 8×8 matrix in Nambu space,

$$\hat{H}_{\text{BdG}} = \begin{pmatrix} \hat{N}_{\mathbf{k}}^{++} & 0 & \hat{\Delta}_{\mathbf{k}}^{+-} & \hat{\Delta}_{\mathbf{k}}^{+-} \\ 0 & \hat{N}_{\mathbf{k}}^{--} & \hat{\Delta}_{\mathbf{k}}^{-+} & \hat{\Delta}_{\mathbf{k}}^{--} \\ [\hat{\Delta}_{\mathbf{k}}^{++}]^\dagger & [\hat{\Delta}_{\mathbf{k}}^{-+}]^\dagger & -\hat{N}_{-\mathbf{k}}^{++} & 0 \\ [\hat{\Delta}_{\mathbf{k}}^{+-}]^\dagger & [\hat{\Delta}_{\mathbf{k}}^{--}]^\dagger & 0 & -\hat{N}_{-\mathbf{k}}^{--} \end{pmatrix}, \quad (17)$$

where the diagonal entries are the normal state dispersion relations $\hat{N}_{\mathbf{k}}^{\nu\nu} = \text{diag}(E_{\mathbf{k},+}^\nu, E_{\mathbf{k},-}^\nu)$ with $\nu = \pm$. Note that $E_{\mathbf{k},\pm}^+$ ($E_{\mathbf{k},\pm}^-$) refer to the upper (lower) spin-split bands, which predominantly exhibit Al (Au) orbital character for small momenta, as can be seen in Fig. 2. Furthermore, the off-diagonal block in \hat{H}_{BdG} is the pairing matrix projected onto the band basis (cf. Appendix C) as obtained by

$$\hat{V}_{\mathbf{k}}^\dagger \text{diag}(\Delta i\hat{\sigma}_y, 0) \hat{V}_{-\mathbf{k}}^{\dagger T} = \begin{pmatrix} \hat{\Delta}_{\mathbf{k}}^{+-} & \hat{\Delta}_{\mathbf{k}}^{+-} \\ \hat{\Delta}_{\mathbf{k}}^{-+} & \hat{\Delta}_{\mathbf{k}}^{--} \end{pmatrix}, \quad (18)$$

where $\hat{V}_{\mathbf{k}}$ is the matrix of eigenvectors associated with the eigenvalue $\hat{\mathcal{E}}_{\mathbf{k}}$ of the normal state Hamiltonian. $\hat{\Delta}_{\mathbf{k}}^{++}$ ($\hat{\Delta}_{\mathbf{k}}^{--}$) correspond to the intraband pairing matrices, specifically pairing between $E_{\mathbf{k},+}^+$ and $E_{\mathbf{k},-}^+$ ($E_{\mathbf{k},+}^-$ and $E_{\mathbf{k},-}^-$) with their hole counterparts leading to the superconducting gap for Al, i.e., δ_{Al} , and the proximity-induced pairing gaps labeled by (δ_{Au}^\pm) in Fig. 4. Such matrices are explicitly given by the relation

$$\hat{\Delta}_{\mathbf{k}}^{\nu\nu} = \frac{i\Delta}{2} \begin{pmatrix} 0 & 1 + \nu G_{\mathbf{k}}^- \\ -1 - \nu G_{\mathbf{k}}^+ & 0 \end{pmatrix}, \quad (19)$$

where $\nu = + (-)$ and

$$G_{\mathbf{k}}^\pm = \frac{\mathcal{E}_{\text{Al}} - \mathcal{E}_{\text{Au}}^\pm}{\sqrt{[\mathcal{E}_{\text{Al}} - \mathcal{E}_{\text{Au}}^\pm]^2 + 4F_0^2}}. \quad (20)$$

In Eq. (18), $\hat{\Delta}_{\mathbf{k}}^{+-}$ ($\hat{\Delta}_{\mathbf{k}}^{-+}$) indicates the interorbital pairing, i.e., pairing between electron bands $E_{\mathbf{k},+}^+$ and $E_{\mathbf{k},-}^+$ with hole band bands $-E_{-\mathbf{k},+}^-$ and $-E_{-\mathbf{k},-}^-$. This gives rise to the emergence of finite-energy Cooper pairing resulting in avoided crossings at finite excitation energy (δ_{IOP}^\pm) in Figs. 4(c) and 4(d). The explicit form for the interband pairing matrix is given by

$$\hat{\Delta}_{\mathbf{k}}^{+-} = \Delta F_0^2 \begin{pmatrix} 0 & \frac{-4i}{\Lambda_{\mathbf{k},1}^- \Lambda_{\mathbf{k},2}^+} \\ \frac{4i}{\Lambda_{\mathbf{k},1}^+ \Lambda_{\mathbf{k},2}^-} & 0 \end{pmatrix}, \quad (21)$$

with

$$\Lambda_{\mathbf{k},l}^\pm = \sqrt{(\mathcal{E}_{\text{Al}} - \mathcal{E}_{\text{Au}}^\pm)^2 (1 + (-1)^l / G_{\mathbf{k}}^\pm)^2 + 4F_0^2}, \quad (22)$$

where $l = \{1, 2\}$. Importantly, the interplay between band hybridization and superconductivity, manifested by ΔF_0^2 in Eq. (21), intrinsically allows for the emergence of finite-energy pairing. Therefore, the interorbital pairing is not induced solely by superconducting order but also by band hybridization in the normal state. This is the answer to question (Q.1).

D. Pairing symmetry analysis

To determine the pairing symmetry in the hybrid structure, it is essential to establish an effective formalism that concentrates on either low *or* finite excitation energies. In this respect, it is necessary to derive a 4×4 matrix formalism from the full 8×8 BdG Hamiltonian \hat{H}_{BdG} . This can be done by utilizing the downfolding method specified in Appendix D. The downfolding method yields the effective model that enables us to investigate the superconducting properties within a given set of energy bands. As mentioned above, there are three distinct sets of spin-split bands where pairing occurs. These bands are characterized by $\nu = \nu' = +(-)$, indicating that the pairing takes place at the Fermi energy, where the energy bands possess predominant Al (Au) orbital character. Another set of bands corresponds to the interorbital bands, where Al-dominated states intersect with Au-dominated hole states (and vice versa). Thus, the general form for the 4×4 effective superconducting Hamiltonian becomes

$$\hat{H}_{\mathbf{k},\text{eff}}^{+\iota} = \begin{pmatrix} \hat{N}_{\mathbf{k}}^{++} + \hat{\xi}_1 & \hat{\Delta}_{\mathbf{k},\text{eff}}^{+\iota} \\ [\hat{\Delta}_{\mathbf{k},\text{eff}}^{+\iota}]^\dagger & -\hat{N}_{-\mathbf{k}}^{\iota\iota} + \hat{\xi}_2 \end{pmatrix}, \quad (23)$$

where the diagonal entries $\hat{\xi}_{1(2)}$ are the energy shifts arising from multiband effects given by

$$\hat{\xi}_1 = \hat{\Delta}_{\mathbf{k}}^{+\nu} \frac{1}{\omega + \hat{N}_{-\mathbf{k}}^{\nu\nu}} [\hat{\Delta}_{\mathbf{k}}^{+\nu}]^\dagger, \quad (24)$$

$$\hat{\xi}_2 = [\hat{\Delta}_{\mathbf{k}}^{-\iota}]^\dagger \frac{1}{\omega - \hat{N}_{\mathbf{k}}^{\iota\iota}} \hat{\Delta}_{\mathbf{k}}^{-\iota}, \quad (25)$$

and ω is a constant. In addition, the effective pairing matrix in Eq. (23) becomes

$$\hat{\Delta}_{\mathbf{k},\text{eff}}^{+\iota} = \hat{\Delta}_{\mathbf{k}}^{+\iota} + \hat{\Delta}_{\mathbf{k}}^{+\nu} \frac{1}{\omega + \hat{N}_{-\mathbf{k}}^{\nu\nu}} [\hat{\Delta}_{\mathbf{k}}^{-\nu}]^\dagger \frac{1}{\omega - \hat{N}_{\mathbf{k}}^{\iota\iota}} \hat{\Delta}_{\mathbf{k}}^{-\iota}. \quad (26)$$

The effective intraorbital (interorbital) superconducting Hamiltonian, i.e., $\hat{H}_{\mathbf{k},\text{eff}}^{++(+-)}$, can be obtained by setting $\iota = +(-)$ and $\nu = -(+)$. Note that $\hat{H}_{\mathbf{k},\text{eff}}^{--}$ can also be derived by substituting $(+) \leftrightarrow (-)$, and setting $\iota = -$ and $\nu = +$ in Eqs. (23)–(26). The spectra of the effective superconducting Hamiltonians $\hat{H}_{\mathbf{k},\text{eff}}^{++}$, $\hat{H}_{\mathbf{k},\text{eff}}^{--}$, and $\hat{H}_{\mathbf{k},\text{eff}}^{+-}$ are obtained numerically and depicted in Figs. 5(a)–5(c). Additionally, the magnitudes of the pseudo-spin-singlet and triplet components corresponding to these spectra are illustrated in Figs. 5(d)–5(f) [61].

Importantly, the proximity-induced intra- and interorbital pairing states are mixtures of singlet and triplet states due to broken inversion symmetry in the Au layer. Based on our model, only the z -component of the \mathbf{d} vector, i.e., $\hat{\Delta}_{\mathbf{k},\text{eff}}^{+\iota}(i\hat{\sigma}_y)^{-1} = \varphi_{\mathbf{k}}^{+\iota}\hat{\sigma}_0 + \mathbf{d}_{\mathbf{k}}^{+\iota} \cdot \hat{\sigma}$, either at the Fermi energy or finite excitation energies, is present. According to Eqs. (19) and (21), the pairing matrices are off-diagonal. Therefore, $\hat{\Delta}_{\mathbf{k},\text{eff}}^{+\iota}$ becomes an off-diagonal matrix reflecting an effective mixed-pairing state having nonvanishing pseudo-spin-singlet $\varphi_{\mathbf{k}}^{\nu\nu}$ and pseudo-spin-triplet $d_{\mathbf{k},z}^{\nu\nu}$ character obtained as

$$\varphi_{\mathbf{k}}^{\nu\nu} = \frac{i\Delta}{4} [2 + \nu(G_{\mathbf{k}}^- + G_{\mathbf{k}}^+)], \quad (27)$$

$$d_{\mathbf{k},z}^{\nu\nu} = \frac{i\Delta}{4} \nu [G_{\mathbf{k}}^- - G_{\mathbf{k}}^+]. \quad (28)$$

where $\nu \in \{+, -\}$. Note that we have excluded terms proportional to the third order of Δ in Eqs. (27) and (28) as they

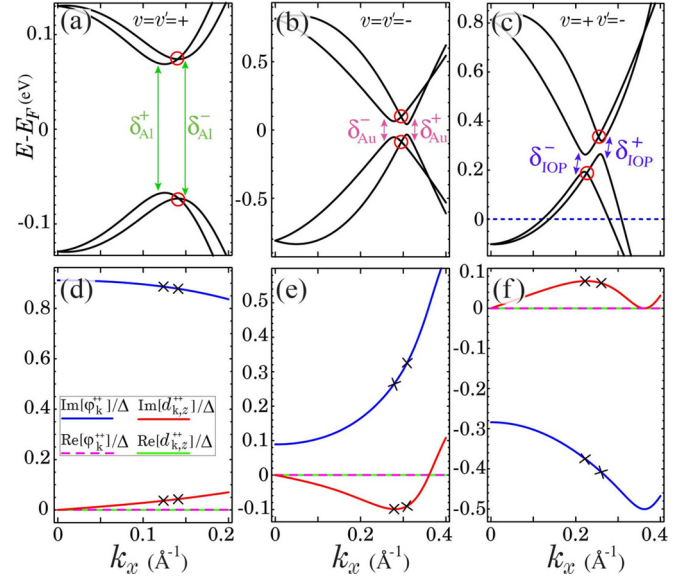


FIG. 5. Effective superconducting excitation spectra for (a) $\hat{H}_{\mathbf{k},\text{eff}}^{++}$ with $\Delta = 0.4F_0$, (b) $\hat{H}_{\mathbf{k},\text{eff}}^{--}$ with $\Delta = 0.8F_0$ (Δ is scaled up for the sake of clarity), and (c) $\hat{H}_{\mathbf{k},\text{eff}}^{+-}$ with $\Delta = 0.4F_0$. (d)–(f) Real and imaginary part of the pseudo-spin-singlet and pseudo-spin-triplet components of the effective pairing matrix associated with the dispersion relation illustrated in the top panels. Black crosses in (d)–(f) highlight k -points where particle and hole bands cross in the absence of pairing. The model parameters are the same as those given in Table I.

are negligibly small in the weak pairing limit. It is worth mentioning that the property $G_{-\mathbf{k}}^\pm = G_{\mathbf{k}}^\mp$ leads to even (odd) parity for the pseudo-spin-singlet (triplet) state, i.e., $\varphi_{-\mathbf{k}}^{\nu\nu} = \varphi_{\mathbf{k}}^{\nu\nu}$ ($d_{-\mathbf{k},z}^{\nu\nu} = -d_{\mathbf{k},z}^{\nu\nu}$). The interorbital pairing components take the form

$$\varphi_{\mathbf{k}}^{+-} = \Delta F_0^2 \left(\frac{-2i}{\Lambda_{\mathbf{k},1}^- \Lambda_{\mathbf{k},2}^-} - \frac{2i}{\Lambda_{\mathbf{k},1}^+ \Lambda_{\mathbf{k},2}^+} \right), \quad (29)$$

$$d_{\mathbf{k},z}^{+-} = \Delta F_0^2 \left(\frac{-2i}{\Lambda_{\mathbf{k},1}^- \Lambda_{\mathbf{k},2}^-} + \frac{2i}{\Lambda_{\mathbf{k},1}^+ \Lambda_{\mathbf{k},2}^+} \right). \quad (30)$$

Overall, we observe that the pseudo-spin-singlet component is consistently larger in magnitude than the triplet component; see Figs. 5(d)–5(f). Note that the pairing state becomes purely pseudo-spin-singlet in the absence of either band hybridization or Rashba spin-orbit coupling, i.e., when $F_0 = 0$ or $\lambda = g = 0$. Therefore, the pseudo-spin-triplet component originates from the interplay between Rashba surface states and band hybridization.

The size of the avoided crossing in the spectrum of the effective pairing Hamiltonian, as expressed in Eq. (23), is given by

$$\delta_{\mathbf{k},\pm}^{\nu\nu'} = \sqrt{|\varphi_{\mathbf{k}}^{\nu\nu'}|^2 + |d_{\mathbf{k},z}^{\nu\nu'}|^2 \pm |(\varphi_{\mathbf{k}}^{\nu\nu'})^* d_{\mathbf{k},z}^{\nu\nu'} + \varphi_{\mathbf{k}}^{\nu\nu'} (d_{\mathbf{k},z}^{\nu\nu'})^*|}, \quad (31)$$

where the third term effectively accounts for the anisotropy observed in the magnitude of the avoided crossing, as initially demonstrated in the KS-BdG simulation in Figs. 4 and 5. This point addresses question (Q.2). Note that the Fermi surface of the hybrid structure consists of four circular rings. The inner

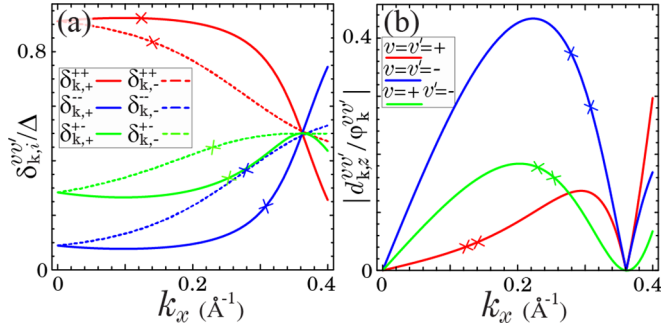


FIG. 6. (a) Magnitude of the effective superconducting avoided crossings for different pairing potentials. (b) Strength of pseudo-spin-triplet $d_{\mathbf{k},z}^{vv'}$ compared to pseudo-spin-singlet $\varphi_{\mathbf{k},z}^{vv'}$ for the effective intraorbital pairing potential, namely $\hat{\Delta}_{\mathbf{k},\text{eff}}^{++}$ and $\hat{\Delta}_{\mathbf{k},\text{eff}}^{--}$, as well as the interorbital pairing potential $\hat{\Delta}_{\mathbf{k},\text{eff}}^{+-}$. The cross marks indicate the momenta where electron and hole bands are crossed in the absence of pairing.

rings are primarily composed of spin-split Al states, while they are surrounded by predominantly spin-split Au states. The superconducting hybridization happens at four Fermi momenta, i.e.,

$$|\mathbf{k}^F| \in \{k_1^{\text{Al}}, k_2^{\text{Al}}, k_1^{\text{Au}}, k_2^{\text{Au}}\} \quad (32)$$

$$= \pm\{0.124, 0.141, 0.278, 0.308\} \text{ \AA}^{-1}. \quad (33)$$

At the above momenta, we have defined the following quantities:

$$\delta_{\text{Al}} \equiv \delta_{k_1^{\text{Al}},+}^{++} \approx \delta_{k_2^{\text{Al}},-}^{++}, \quad \delta_{\text{Au}}^- \equiv \delta_{k_1^{\text{Au}},-}^{--}, \quad \delta_{\text{Au}}^+ \equiv \delta_{k_2^{\text{Au}},+}^{--}. \quad (34)$$

Therefore, the full pairing gap for the hybrid structure at the Fermi energy can be determined by $\delta_{\text{Au}}^+ = \min(\delta_{\text{Al}}, \delta_{\text{Au}}^-, \delta_{\text{Au}}^+)$. The interorbital Cooper pairing away from the Fermi energy happens at momenta $k_1^{\text{IOP}} = 0.221 \text{ \AA}^{-1}$ and $k_2^{\text{IOP}} = 0.26 \text{ \AA}^{-1}$. Accordingly, the magnitude of finite-energy Cooper pairing is defined by $\delta_{\text{IOP}}^- \equiv \delta_{k_1^{\text{IOP}},-}^{+-}$ and $\delta_{\text{IOP}}^+ \equiv \delta_{k_2^{\text{IOP}},+}^{+-}$.

The magnitudes of both intra- and interorbital pairings are plotted in Fig. 6(b). Apparently, the intraorbital bands labeled by $\nu = \nu' = + (-)$ exhibit the largest (smallest) pairing gap at low momenta, indicating a dominant Al (Au) orbital character. Interestingly, the interorbital pairing leads to larger avoided crossings compared to the intraorbital pairing of predominantly Au electrons. The Fermi momenta for the intraorbital energy bands are marked in blue and red crosses at $k = 0.124, 0.141, 0.278,$ and 0.308 \AA^{-1} , respectively. At these momenta, the pairing anisotropy for Al-dominated states is slightly larger than the energy bands with dominant Au orbital character. Importantly, we observe that the pairing anisotropy disappears at critical momenta $k_c = 0.368 \text{ \AA}^{-1}$, resulting in identical sizes for the pairing potentials. This occurs because the induced intra- and interorbital pairing becomes a purely pseudo-spin-singlet state by eliminating the spin-split nature of the bands, specifically, $d_{\mathbf{k},z}^{++} = d_{\mathbf{k},z}^{--} = d_{\mathbf{k},z}^{+-} = 0$. The critical momenta can be determined by setting $\mathcal{E}_{\text{Al}} - \mathcal{E}_{\text{Au}}^{\pm} = 0$ according to Eqs. (20) and (22). In general, the proximity-induced pairing exhibits a stronger presence of the pseudo-spin-singlet component over the triplet component,

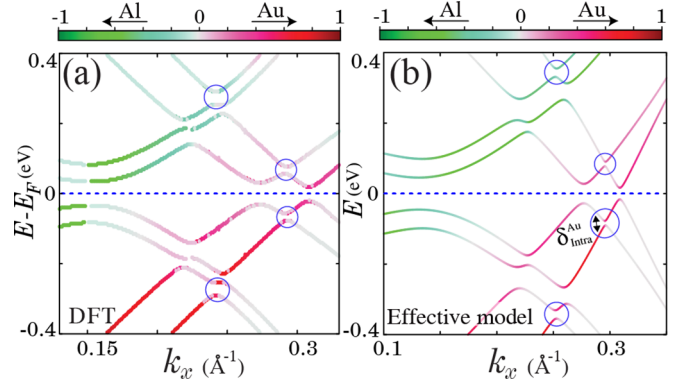


FIG. 7. Superconducting band structure of Al/Au obtained by (a) DFT calculations and (b) analytical model in the presence of Zeeman magnetic field of size $B = 2 \text{ mRy}$. Finite-energy Cooper pairings, highlighted by blue circles, emerge due to the interplay between superconductivity and magnetic field. The color bar indicates particle (red/green) and hole (gray) components of the BdG spectra. The model parameters for the analytical model are those given in Table I and $\Delta = 0.4F_0$.

i.e., $d_{\mathbf{k},z}^{vv'}/\varphi_{\mathbf{k}}^{vv'} < 1$, as illustrated in Fig. 6(a). This answers question (Q.3). Notably, among the various pairing potentials, the Au-dominated states, labeled by $\nu = \nu' = -$, display the largest contribution from the triplet component.

E. Finite-energy interorbital avoided crossing with external magnetic fields

Note that we do not observe the occurrence of an interband pairing between the two dominant Rashba states displaying opposite spin-polarization marked by black and red circles in Figs. 4 and 5, respectively. These crossings are protected by time-reversal and spin-rotational symmetries. They can, however, be lifted if an external Zeeman field is applied to the heterostructure. This point answers question (Q.4).

The effect of an external magnetic field on the electronic structure is shown in Fig. 7, both from DFT and low-energy model perspectives. As the Zeeman field strength increases, the Rashba spin-split bands undergo further splitting. This shift of the bands leads to a decreasing superconducting energy gap in predominant Al states because spin-up and spin-down states are shifted away from each other. For large external magnetic fields, the gap closes completely and superconductivity is destroyed at the critical field of the superconductor. Note that the interband pairing between particle-hole Rashba states at finite excitation energy is clearly visible before the superconducting gap for Al states closes.

IV. DISCUSSION AND CONCLUSION

Our results show the existence of finite-energy pairing due to the complex multiband effects arising in the proximity effect of heterostructures between s -wave superconductors and heavy metals hosting Rashba surface states. The main ingredients are as follows:

- (i) s -wave superconductivity.
- (ii) Surface states originating from the normal metal.
- (iii) Rashba SOC in the normal metal.

TABLE II. Superconducting energy gap, critical temperature, and critical magnetic field of Al of different film thicknesses.

δ (μeV)	T_c (K)	H_c (T)	References
208–307	1.2–2.8	0.01–5	Ref. [64] Ref. [63]

(iv) Significant hybridization between Rashba surface states and the electronic structure of the s -wave superconductor.

If all these requirements are met, finite-energy pairing emerges between discrete states of the superconductor and the Rashba surface states. This unconventional pairing leads to avoided crossings in the BdG band structures. In our case, discrete states in the superconductor are pronounced due to finite-size effects of the thin Al films. Their location relative to the position of the Au surface states can be fine-tuned by appropriate doping or film thickness. This allows us to control at which finite energy the interorbital pairing between Al and Au Rashba states occurs. It is important to note that finite-energy pairing only appears in thin Al films since in the semi-infinite limit no discrete quantum-well states are present (see Appendix F).

The size of the observable avoided crossings for the Al/Au heterostructure depends crucially on the superconducting gap of the superconductor (summarized in Tables II and III). Aluminum has a critical temperature of $T_c \approx 1$ K and a critical magnetic field of $H_c \approx 10$ mT [62]. In the thin-film limit, both T_c and H_c increase substantially [63–65], together with an increased size of the superconducting gap of $\delta_{\text{Al}} \approx 300 \mu\text{eV}$ [64]. The proximity-induced pairings at zero (within the Au Rashba bands) and finite excitation energy (due to Al-Au interorbital pairing) are of size $\delta_{\text{IOP}}^{\pm} \approx 100\text{--}200 \mu\text{eV}$. The Au-Au interorbital avoided crossing that only opens up under a finite magnetic field is of size $\delta_{\text{intra}}^{\text{Au}} \approx 30\text{--}50 \mu\text{eV}$ for values of the magnetic field well below the critical field of Al. To resolve this experimentally, an energy resolution of $\Delta_E \approx 10\text{--}20 \mu\text{eV}$ should suffice. If we assume a thermal broadening of $3.5k_B T$, we can estimate that experiments need to be performed at $T = \Delta_E / (3.5k_B) \approx 30\text{--}60$ mK in order to be able to resolve Δ_E . With state-of-the-art STM and transport experiments in dilution refrigerators, energy resolutions below $10 \mu\text{eV}$ at operating temperatures of 10 mK are indeed possible [66]. Thus, we believe that our predicted finite-energy features in the superconducting electronic structure of Au/Al are observable.

Suitable materials engineering might further enhance the chances to detect and eventually exploit finite-energy pairings. A strong Rashba effect is typically seen in p -electron materi-

TABLE III. Finite-energy avoided crossings (δ in μeV) from DFT. The numbers are scaled values using a value of the superconducting gap of Al of $\delta_{\text{Al}} = 300 \mu\text{eV}$ for very thin films [64].

	δ_{Au}^-	δ_{Au}^+	δ_{IOP}^-	δ_{IOP}^+	$\delta_{\text{IOP}}^{\text{Au}}$	$\delta_{\text{IOP}}^{\text{Au}}$	$\delta_{\text{IOP}}^{\text{Au}}$
δ	114	153	180	132	0	31	52
H/H_c	0	0	0	0	0	~ 0.3	~ 0.4

als. Superconductors whose electronic structure close to the Fermi level is dominated by sp -electrons, as is the case for Al, are therefore well suited to achieve strong hybridization with Rashba materials. Consequently, other superconductors with larger superconducting gaps (e.g., Pb with $T_c \approx 7.2$ K), that nevertheless have dominating p -electron character responsible for superconductivity, are promising to increase the observable size of the finite-energy pairing. Furthermore, replacing Au by the Bi/Ag(111) surface alloy, which shows a gigantic Rashba effect [26], is another option for optimization. Apart from Rashba-type SOC, also bulk-inversion asymmetric crystals (e.g., BiTeI or IrBiSe [67,68]), where additionally Dresselhaus-type SOC-induced spin-momentum locking can be present, could be explored in this context. Observing finite-energy pairing under broken pseudo-spin-rotational symmetry benefits from a material with larger g -factor to increase the response to the magnetic field. InSb nanowires could be interesting systems for this purpose [69]. Moreover, van der Waals heterostructures are rich material combinations where proximity effects and interorbital pairing can be explored [70]. In these systems, the possibility of engineering the band structures via moiré superlattices provides additional knobs to tune their physical properties [71].

Despite the abundance of heterostructures currently under investigation in the context of the search for MZMs or superconducting spintronics, multiband physics in heterostructures remains largely unexplored. A variety of emergent phenomena can be explored in materials that show strong multiband effects. For instance, multiband superconductors can lead to exotic odd-frequency superconductivity [72]. Suitable materials engineering might further promote control over the mixed singlet-triplet character of the finite-energy pairing, which we demonstrate for Al/Au. This could be useful to control spin-triplet superconductivity, which in turn plays a pivotal role in superconducting spintronics [73,74]. Moreover, spin-3/2 superconductors (e.g., YPtBi) or superconductors that show local inversion symmetry breaking in their crystal structures (e.g., CeRh₂As₂) are other examples where multiband physics and broken symmetries inherently lead to unconventional pairing [75,76]. Finally, novel topological superconducting pairing at finite energies [37] is another exciting direction for future research in real materials beyond model-based calculations.

In summary, in our combined DFT and low-energy model approach, we study the proximity effect in a heterostructure of Au with strong Rashba SOC and the s -wave superconductor Al. We show the existence of finite-energy pairing in the superconducting state, and we analyze the mixed singlet-triplet character of the proximity-induced pairing. Combining the strengths of predictive DFT simulations with the insights from model calculations, our results pave the way towards a deeper understanding and experimental detection of multiband effects in superconducting heterostructures.

ACKNOWLEDGMENTS

We acknowledge stimulating discussions with Juba Bouaziz, Julia Link, and Carsten Timm. We thank the Bavarian Ministry of Economic Affairs, Regional Development and Energy for financial support within the High-Tech Agenda

Project “Bausteine für das Quantencomputing auf Basis topologischer Materialien mit experimentellen und theoretischen Ansätzen.” The work was also supported by the SFB1170 ToCoTronics and the Würzburg-Dresden Cluster of Excellence ct.qmat, EXC2147, Project Id 390858490. Furthermore, this work was funded by the Deutsche Forschungsgemeinschaft (DFG, German Research Foundation) under Germany’s Excellence Strategy–Cluster of Excellence Matter and Light for Quantum Computing (ML4Q) EXC 2004/1–390534769. We are also grateful for computing time granted by the JARA Vergabegremium and provided on the JARA Partition part of the supercomputer CLAIX at RWTH Aachen University (Project No. jara0191).

APPENDIX A: COMPUTATIONAL DETAILS OF THE DFT SIMULATIONS

Our density-functional-theory calculations rely on multiple-scattering theory and employ the relativistic Korringa-Kohn-Rostoker Green function method (KKR) [77,78] as implemented in the JuKKR code [49]. We use the local density approximation (LDA) to parametrize the normal state exchange correlation functional [79] and an $\ell_{\max} = 2$ cutoff in the angular momentum expansion of the space-filling Voronoi cells around the atomic centers where we make use of the exact (i.e., full-potential) description of the atomic shapes [80,81]. We use a two-dimensional geometry where periodicity is assumed in the plane, but a finite layer thickness is used in the direction along the heterostructure.

The series of DFT calculations in this study are orchestrated with the help of the AiiDA-KKR plugin [82,83] to the AiiDA infrastructure [84]. This has the advantage that the data provenance is automatically stored in compliance with the FAIR principles of open data [85]. The complete data set that includes the full provenance of the calculations is made publicly available in the materials cloud repository [86,87].

The source codes of the AiiDA-KKR plugin [82,83] and the JuKKR code [49] are published as open source software under the MIT license in Ref. [88].

APPENDIX B: ADDITIONAL DETAILS OF THE NORMAL STATE ELECTRONIC STRUCTURE FROM DFT

Figure 8 shows the total and layer-resolved density of states (DOS) of the Al/Au heterostructure as computed from DFT. The fully occupied d -shell of Au can be seen between $E - E_F = -8$ eV and $E - E_F = -2$ eV, and we confirm the well-known fact that the DOS at E_F has predominantly $s - p_z$ character. The electrons in aluminum show an almost, i.e., except for small van Hove singularities due to lifting of degeneracies in sp -bands by crystal fields, free-electron nature that can be recognized in the typical square-root shape of the DOS.

APPENDIX C: BAND BASIS REPRESENTATION

Using the Gram-Schmidt method, we derive orthonormal eigenvectors for the normal state Hamiltonian given in Eq. (1)

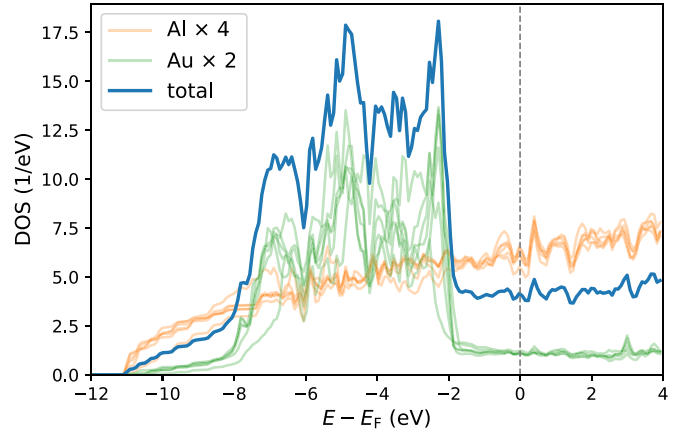


FIG. 8. Density of states of the Al/Au heterostructure. The faint orange and green lines indicate the contributions of the individual Al and Au layers to the total DOS (blue line).

as

$$\hat{\nu}(\mathbf{k}) = \begin{pmatrix} \frac{-i\sqrt{2}\gamma}{2\sqrt{\gamma^2+4F_0^2}} & \frac{i\sqrt{2}P}{2\sqrt{P^2+4F_0^2}} & \frac{i\sqrt{2}v}{2\sqrt{v^2+4F_0^2}} & \frac{-i\sqrt{2}\Omega}{2\sqrt{\Omega^2+4F_0^2}} \\ \frac{\sqrt{\gamma^2+4F_0^2}}{\sqrt{8}\Theta^-} & \frac{\sqrt{P^2+4F_0^2}}{\sqrt{8}\Theta^+} & \frac{-\sqrt{2}v}{2\sqrt{v^2+4F_0^2}} & \frac{\sqrt{\Omega^2+4F_0^2}}{-\sqrt{8}\Theta^+} \\ \frac{-i\sqrt{2}F_0}{\sqrt{\gamma^2+4F_0^2}} & \frac{i\sqrt{2}F_0}{\sqrt{P^2+4F_0^2}} & \frac{-i\sqrt{8}F_0}{2\sqrt{v^2+4F_0^2}} & \frac{i\sqrt{2}F_0}{\sqrt{\Omega^2+4F_0^2}} \\ \frac{\sqrt{2}F_0}{\sqrt{\gamma^2+4F_0^2}} & \frac{\sqrt{2}F_0}{\sqrt{P^2+4F_0^2}} & \frac{\sqrt{8}F_0}{2\sqrt{v^2+4F_0^2}} & \frac{\sqrt{2}F_0}{\sqrt{\Omega^2+4F_0^2}} \end{pmatrix}, \quad (\text{C1})$$

where $[\hat{\nu}(\mathbf{k})]^\dagger \hat{\nu}(\mathbf{k}) = 1$ and we have defined

$$\Theta^+ = \sqrt{(\Upsilon^+)^2 + 4F_0^2}, \quad \Theta^- = \sqrt{(\Upsilon^-)^2 + 4F_0^2}, \quad (\text{C2})$$

$$\Upsilon^+ = \mathcal{E}_{\text{Al}} - \mathcal{E}_{\text{Au}}^+, \quad \Upsilon^- = \mathcal{E}_{\text{Al}} - \mathcal{E}_{\text{Au}}^-, \quad (\text{C3})$$

$$\gamma = \Theta^- + \Upsilon^-, \quad P = \Theta^+ + \Upsilon^+, \quad (\text{C4})$$

$$v = \Theta^- - \Upsilon^-, \quad \Omega = \Theta^+ - \Upsilon^+. \quad (\text{C5})$$

The band basis representation for the BdG Hamiltonian can be obtained as follows. The superconducting Hamiltonian is defined by $H = \sum_{\mathbf{k}} \hat{\psi}_{\mathbf{k}}^\dagger \hat{\mathcal{H}}(\mathbf{k}) \hat{\psi}_{\mathbf{k}}$, where the Nambu basis is $\hat{\psi}_{\mathbf{k}} = (\hat{\phi}_{\mathbf{k}}^\dagger, \hat{\phi}_{-\mathbf{k}}^\dagger)^T$, and the BdG Hamiltonian is given by

$$\hat{\mathcal{H}}(\mathbf{k}) = \begin{pmatrix} \hat{H}(\mathbf{k}) & \text{diag}(\Delta i\hat{\sigma}_y, 0) \\ [\text{diag}(\Delta i\hat{\sigma}_y, 0)]^\dagger & -\hat{H}^T(-\mathbf{k}) \end{pmatrix}, \quad (\text{C6})$$

where $\hat{H}(\mathbf{k})$ is the 4×4 matrix form of the normal state Hamiltonian. The band basis representation of the superconducting Hamiltonian can be obtained through the similarity transformation $\hat{H}_{\text{BdG}}(\mathbf{k}) = \hat{U}^\dagger \hat{\mathcal{H}}(\mathbf{k}) \hat{U}$ with $\hat{U} = \hat{\nu}(\mathbf{k}) \oplus [\hat{\nu}(-\mathbf{k})]^\dagger$.

APPENDIX D: DOWNFOLDING METHOD

In this Appendix, we explain how to employ the downfolding method to obtain a 4×4 effective Hamiltonian to describe spectral properties of the system for a specified energy window. Our starting point is a general superconducting Hamiltonian, represented in the eigenspace of the normal state

given by the 8×8 matrix

$$\hat{H} = \left(\begin{array}{cc|cc} \hat{N}_1 & 0 & \hat{\Delta}_1 & \hat{\Delta}_2 \\ 0 & \hat{N}_2 & \hat{\Delta}_3 & \hat{\Delta}_4 \\ \hline \hat{\Delta}_1^\dagger & \hat{\Delta}_3^\dagger & \hat{h}_1 & 0 \\ \hat{\Delta}_2^\dagger & \hat{\Delta}_4^\dagger & 0 & \hat{h}_2 \end{array} \right), \quad (\text{D1})$$

where $\hat{N}_{1(2)}$ ($\hat{h}_{1(2)}$) is a 2×2 diagonal subblock matrix containing a pair of energy bands in the normal state, and $\hat{\Delta}_{1(4)}$ and $\hat{\Delta}_{2(3)}$ are the pairing matrices projected onto the intraband (interband). Note that $\hat{\Delta}_{1(4)}$ and $\hat{\Delta}_{2(3)}$ induce full and partial pairing gaps at Fermi energy and finite excitation energies, respectively. Without loss of generality, we change the basis of \hat{H} with the unitary transformation \hat{U} to let the diagonal subblocks contain the electron-hole components with a pairing potential. This can be done with $\hat{H}' = \hat{U}^\dagger \hat{H} \hat{U}$, where \hat{U} is given by

$$\hat{U}^{-1} = \hat{U}^\dagger = \begin{pmatrix} 1 & 0 & 0 & 0 \\ 0 & 0 & 0 & 1 \\ 0 & 1 & 0 & 0 \\ 0 & 0 & 1 & 0 \end{pmatrix}, \quad (\text{D2})$$

and \hat{H}' becomes

$$\hat{H}' = \left(\begin{array}{cc|cc} \hat{N}_1 & \hat{\Delta}_2 & 0 & \hat{\Delta}_1 \\ \hat{\Delta}_2^\dagger & \hat{h}_2 & \hat{\Delta}_4^\dagger & 0 \\ \hline 0 & \hat{\Delta}_4 & \hat{N}_2 & \hat{\Delta}_3 \\ \hat{\Delta}_1^\dagger & 0 & \hat{\Delta}_3^\dagger & \hat{h}_1 \end{array} \right) \equiv \left(\begin{array}{c|c} \hat{M}_{11} & \hat{M}_{12} \\ \hline \hat{M}_{21} & \hat{M}_{22} \end{array} \right). \quad (\text{D3})$$

In multiband systems, the downfolding method paves the way to obtain the spectral properties of a desired subblock, e.g., \hat{M}_{11} , taking into account the perturbative effects of other blocks. To understand the method, we consider the eigenvalue problem for H' given by

$$\begin{pmatrix} \hat{M}_{11} & \hat{M}_{12} \\ \hat{M}_{21} & \hat{M}_{22} \end{pmatrix} \begin{pmatrix} \hat{\psi}_A \\ \hat{\psi}_B \end{pmatrix} = E \begin{pmatrix} \hat{\psi}_A \\ \hat{\psi}_B \end{pmatrix}, \quad (\text{D4})$$

where $(\hat{\psi}_A, \hat{\psi}_B)^T$ is the eigenvector associated with eigenenergy E . Equation (D4) is a coupled equation that can be written as

$$\hat{M}_{11} \hat{\psi}_A + \hat{M}_{12} \hat{\psi}_B = E \hat{\psi}_A, \quad (\text{D5})$$

$$\hat{M}_{21} \hat{\psi}_A + \hat{M}_{22} \hat{\psi}_B = E \hat{\psi}_B. \quad (\text{D6})$$

Inserting $\hat{\psi}_B = (E - \hat{M}_{22})^{-1} \hat{M}_{21} \hat{\psi}_A$ into Eq. (D5) results in $\hat{M}_{11}^{\text{eff}} \hat{\psi}_A = E \hat{\psi}_A$ with

$$\hat{M}_{11}^{\text{eff}} = \hat{M}_{11} + \hat{M}_{12} \hat{\Lambda}^{-1} \hat{M}_{21}, \quad (\text{D7})$$

where $\hat{\Lambda} = (\omega \hat{I}_4 - \hat{M}_{22})^{-1}$, \hat{I}_4 is the 4×4 identity matrix, and ω denotes a constant close to the energy range where the desired pairing happens. Thus, eigenvalues $\hat{M}_{11}^{\text{eff}}$ describes the spectral properties of \hat{M}_{11} taking into account the effects of other subblocks. We now aim to find an expression for $\hat{\Lambda}^{-1}$. To do so, we define $\hat{\Lambda} \equiv \hat{\varepsilon} + \hat{\Delta}$, where $\hat{\varepsilon}$ ($\hat{\Delta}$) is the normal state (pairing) part given by

$$\hat{\varepsilon} = \begin{pmatrix} \omega \hat{I}_2 - \hat{N}_2 & 0 \\ 0 & \omega \hat{I}_2 - \hat{h}_1 \end{pmatrix}, \quad (\text{D8})$$

$$\hat{\Delta} = \begin{pmatrix} 0 & -\hat{\Delta}_3 \\ -\hat{\Delta}_3^\dagger & 0 \end{pmatrix}. \quad (\text{D9})$$

We can find the inverse of $\hat{\Lambda}$ using the Neumann series expansion up to second order given by

$$\hat{\Lambda}^{-1} = \hat{\varepsilon}^{-1} (\hat{I} + \hat{\Delta} \hat{\varepsilon}^{-1})^{-1} = \hat{\varepsilon}^{-1} \sum_{n=0}^{\infty} (-\hat{\Delta} \hat{\varepsilon}^{-1})^n \quad (\text{D10})$$

$$\approx \hat{\varepsilon}^{-1} (\hat{I} - \hat{\Delta} \hat{\varepsilon}^{-1}) = \hat{\varepsilon}^{-1} - \hat{\varepsilon}^{-1} \hat{\Delta} \hat{\varepsilon}^{-1} \quad (\text{D11})$$

$$= \begin{pmatrix} \frac{1}{\omega \hat{\sigma}_0 - \hat{N}_2} & \frac{1}{\omega \hat{\sigma}_0 - \hat{N}_2} \hat{\Delta}_3 \frac{1}{\omega \hat{\sigma}_0 - \hat{h}_1} \\ \frac{1}{\omega \hat{\sigma}_0 - \hat{h}_1} [\hat{\Delta}_3]^\dagger \frac{1}{\omega \hat{\sigma}_0 - \hat{N}_2} & \frac{1}{\omega \hat{\sigma}_0 - \hat{h}_1} \end{pmatrix}. \quad (\text{D12})$$

Note that Eq. (D10) converges when the norm of $\hat{\Delta} \hat{\varepsilon}^{-1}$ is smaller than unity, which can be fulfilled in the weak pairing limit. After some algebra, we arrive at an explicit relation for $\hat{M}_{11}^{\text{eff}}$ that is

$$\hat{M}_{11}^{\text{eff}} = \begin{pmatrix} \hat{N}_1 + \hat{\xi}_1 & \hat{\Delta}_2^{\text{eff}} \\ [\hat{\Delta}_2^{\text{eff}}]^\dagger & \hat{h}_2 + \hat{\xi}_2 \end{pmatrix}, \quad (\text{D13})$$

where the energy shifts arising from the multiband nature as

$$\hat{\xi}_1 = \hat{\Delta}_1 \frac{1}{\omega \hat{\sigma}_0 - \hat{h}_1} \hat{\Delta}_1^\dagger, \quad (\text{D14})$$

$$\hat{\xi}_2 = \hat{\Delta}_4^\dagger \frac{1}{\omega \hat{\sigma}_0 - \hat{N}_2} \hat{\Delta}_4. \quad (\text{D15})$$

Additionally, the effective 2×2 pairing matrix takes the form

$$\hat{\Delta}_2^{\text{eff}} = \hat{\Delta}_2 + \hat{\Delta}_1 \frac{1}{\omega \hat{\sigma}_0 - \hat{h}_1} \hat{\Delta}_3^\dagger \frac{1}{\omega \hat{\sigma}_0 - \hat{N}_2} \hat{\Delta}_4. \quad (\text{D16})$$

According to Eqs. (16) and (24), the projected pairing matrices $\hat{\Delta}_{1,2,3,4}$ have only nonvanishing off-diagonal elements, and also $\hat{N}_1 + \hat{\xi}_1 \equiv \text{diag}(\zeta_1, \zeta_2)$ and $\hat{h}_2 + \hat{\xi}_2 \equiv \text{diag}(\zeta_3, \zeta_4)$ are diagonal matrices due to time-reversal symmetry. In this case, $\hat{\Delta}_2^{\text{eff}}$ becomes an off-diagonal matrix explicitly given by

$$\hat{\Delta}_2^{\text{eff}} = \begin{pmatrix} 0 & (\hat{\Delta}_2)_{12} + \frac{(\hat{\Delta}_1)_{12} [(\hat{\Delta}_3)_{12}]^* (\hat{\Delta}_4)_{12}}{[\omega - (\hat{h}_1)_{22}] [\omega - (\hat{N}_2)_{11}]} \\ (\hat{\Delta}_2)_{21} + \frac{(\hat{\Delta}_1)_{21} [(\hat{\Delta}_3)_{21}]^* (\hat{\Delta}_4)_{21}}{[\omega - (\hat{h}_1)_{11}] [\omega - (\hat{N}_2)_{22}]} & 0 \end{pmatrix}, \quad (\text{D17})$$

where $(\)_{ij}$ indicates the matrix element of the given matrix. To find the pairing symmetry for $\hat{\Delta}_2^{\text{eff}}$, we can multiply it with the inverse of the Cooper pair symmetrization factor, i.e., $(i\hat{\sigma}_y)^{-1}$ leading to the effective pseudo-spin-singlet (φ) and

pseudo-spin-triplet (\mathbf{d} -vector) components, i.e., $\hat{\Delta}_2^{\text{eff}} (i\hat{\sigma}_y)^{-1} = \varphi \hat{\sigma}_0 + \mathbf{d} \cdot \hat{\sigma}$. In our model, $\hat{\Delta}_2^{\text{eff}}$ is off-diagonal reflecting an effective mixed pairing state having nonvanishing pseudo-spin-singlet and triplet components of the \mathbf{d} -vector explicitly

given by

$$\varphi = \frac{1}{2} \left((\hat{\Delta}_2)_{12} - (\hat{\Delta}_2)_{21} + \frac{(\hat{\Delta}_1)_{12}[(\hat{\Delta}_3)_{12}]^*(\hat{\Delta}_4)_{12}}{[\omega - (\hat{h}_1)_{22}][\omega - (\hat{N}_2)_{11}]} - \frac{(\hat{\Delta}_1)_{21}[(\hat{\Delta}_3)_{21}]^*(\hat{\Delta}_4)_{21}}{[\omega - (\hat{h}_1)_{11}][\omega - (\hat{N}_2)_{22}]}, \right) \quad (\text{D18})$$

$$d_z = \frac{1}{2} \left((\hat{\Delta}_2)_{12} + (\hat{\Delta}_2)_{21} + \frac{(\hat{\Delta}_1)_{12}[(\hat{\Delta}_3)_{12}]^*(\hat{\Delta}_4)_{12}}{[\omega - (\hat{h}_1)_{22}][\omega - (\hat{N}_2)_{11}]} + \frac{(\hat{\Delta}_1)_{21}[(\hat{\Delta}_3)_{21}]^*(\hat{\Delta}_4)_{21}}{[\omega - (\hat{h}_1)_{11}][\omega - (\hat{N}_2)_{22}]}. \right) \quad (\text{D19})$$

Considering Eqs. (D18) and (D19), $\hat{M}_{11}^{\text{eff}}$ becomes

$$\hat{M}_{11}^{\text{eff}} = \begin{pmatrix} \zeta_1 & 0 & 0 & d_z + \varphi \\ 0 & \zeta_2 & d_z - \varphi & 0 \\ 0 & d_z^* - \varphi^* & \zeta_3 & 0 \\ d_z^* + \varphi^* & 0 & 0 & \zeta_4 \end{pmatrix}. \quad (\text{D20})$$

Interestingly, $\hat{M}_{11}^{\text{eff}}$ can preserve pseudo-spin-rotational symmetry. The matrix form for such an operator is defined by

$$\hat{D}_{\mathbf{n}}(\theta) \equiv \text{diag}(e^{i\theta/2(\mathbf{n}\cdot\hat{\sigma})}, e^{-i\theta/2(\mathbf{n}\cdot\hat{\sigma})^*}), \quad (\text{D21})$$

where θ is the angle of rotation in the pseudospin space. Note that $\hat{M}_{11}^{\text{eff}}$ preserves pseudo-spin- π rotational symmetry along the z -axis, i.e., $[\hat{M}_{11}^{\text{eff}}, \hat{D}_{n_z}(\pi)] = 0$, with

$$\hat{D}_{n_z}(\pi) = \begin{pmatrix} i & 0 & 0 & 0 \\ 0 & -i & 0 & 0 \\ 0 & 0 & -i & 0 \\ 0 & 0 & 0 & i \end{pmatrix}. \quad (\text{D22})$$

Representing $\hat{M}_{11}^{\text{eff}}$ in the eigenspace of $\hat{D}_{n_z}(\pi)$ denoted by \hat{U} , we decouple the effective Hamiltonian into two sectors given by

$$\hat{\mathcal{M}}_{11}^{\text{eff}} = \hat{U}^{-1} \hat{M}_{11}^{\text{eff}} \hat{U} = \text{diag}(\hat{\mathcal{H}}_1, \hat{\mathcal{H}}_2), \quad (\text{D23})$$

where

$$\hat{\mathcal{H}}_1 = \begin{pmatrix} \zeta_4 & d_z^* + \varphi^* \\ d_z + \varphi & \zeta_1 \end{pmatrix}, \quad (\text{D24})$$

$$\hat{\mathcal{H}}_2 = \begin{pmatrix} \zeta_3 & d_z^* - \varphi^* \\ d_z - \varphi & \zeta_4 \end{pmatrix}. \quad (\text{D25})$$

Therefore, the effective superconducting spectra become

$$E = \frac{1}{2}(\zeta_1 + \zeta_4 \pm \sqrt{(\zeta_1 - \zeta_4)^2 + 4\delta^2}), \quad (\text{D26})$$

where the magnitude of the avoided crossing is

$$\delta = \sqrt{|\varphi|^2 + |d_z|^2 \pm (\varphi^* d_z + \varphi d_z^*)}. \quad (\text{D27})$$

APPENDIX E: EFFECTIVE LOW-ENERGY THEORY

In this Appendix, we employ the general formalism of the downfolding method, described in Appendix D, to obtain an effective low (finite) -energy intraband (interband) superconducting Hamiltonian for the Al/Au model. We first derive the low-energy formalism while the finite-energy pairing is formulated subsequently.

1. Band basis label with $\nu = \nu' = +$

Consider the BdG Hamiltonian represented in the eigenspace of the normal state model given by

$$\hat{\mathcal{H}}_{\mathbf{k}} = \begin{pmatrix} \hat{N}_{\mathbf{k}}^{++} & 0 & \hat{\Delta}_{\mathbf{k}}^{++} & \hat{\Delta}_{\mathbf{k}}^{+-} \\ 0 & \hat{N}_{\mathbf{k}}^{--} & \hat{\Delta}_{\mathbf{k}}^{+-} & \hat{\Delta}_{\mathbf{k}}^{--} \\ [\hat{\Delta}_{\mathbf{k}}^{++}]^\dagger & [\hat{\Delta}_{\mathbf{k}}^{+-}]^\dagger & -\hat{N}_{-\mathbf{k}}^{++} & 0 \\ [\hat{\Delta}_{\mathbf{k}}^{+-}]^\dagger & [\hat{\Delta}_{\mathbf{k}}^{--}]^\dagger & 0 & -\hat{N}_{-\mathbf{k}}^{--} \end{pmatrix}. \quad (\text{E1})$$

To derive the effective superconducting Hamiltonian at the Fermi energy, we change the basis to an intraband formalism through a unitary transformation $\hat{\mathcal{H}}_{\mathbf{k}}' = \hat{U}'^\dagger \hat{\mathcal{H}}_{\mathbf{k}} \hat{U}'$, where \hat{U}' is given by

$$(\hat{U}')^{-1} = \hat{U}'^\dagger = \begin{pmatrix} 1 & 0 & 0 & 0 \\ 0 & 0 & 1 & 0 \\ 0 & 1 & 0 & 0 \\ 0 & 0 & 0 & 1 \end{pmatrix}, \quad (\text{E2})$$

and $\hat{\mathcal{H}}_{\mathbf{k}}'$ becomes

$$\hat{\mathcal{H}}_{\mathbf{k}}' = \left(\begin{array}{cc|cc} \hat{N}_{\mathbf{k}}^{++} & \hat{\Delta}_{\mathbf{k}}^{++} & 0 & \hat{\Delta}_{\mathbf{k}}^{+-} \\ [\hat{\Delta}_{\mathbf{k}}^{++}]^\dagger & -\hat{N}_{-\mathbf{k}}^{++} & [\hat{\Delta}_{\mathbf{k}}^{+-}]^\dagger & 0 \\ \hline 0 & \hat{\Delta}_{\mathbf{k}}^{+-} & \hat{N}_{-\mathbf{k}}^{--} & \hat{\Delta}_{\mathbf{k}}^{--} \\ [\hat{\Delta}_{\mathbf{k}}^{+-}]^\dagger & 0 & [\hat{\Delta}_{\mathbf{k}}^{--}]^\dagger & -\hat{N}_{-\mathbf{k}}^{--} \end{array} \right). \quad (\text{E3})$$

The first 4×4 block describes the superconducting sector with predominant aluminum orbital character in the normal state for small momenta. Comparing Eq. (E3) with Eq. (D3), we deduce that

$$\hat{N}_1 = \hat{N}_{\mathbf{k}}^{++}, \quad \hat{h}_2 = -\hat{N}_{-\mathbf{k}}^{++}, \quad (\text{E4})$$

$$\hat{N}_2 = \hat{N}_{\mathbf{k}}^{--}, \quad \hat{h}_1 = -\hat{N}_{-\mathbf{k}}^{--}, \quad (\text{E5})$$

$$\hat{\Delta}_1 = \hat{\Delta}_{\mathbf{k}}^{+-}, \quad \hat{\Delta}_2 = \hat{\Delta}_{\mathbf{k}}^{++}, \quad (\text{E6})$$

$$\hat{\Delta}_3 = \hat{\Delta}_{\mathbf{k}}^{--}, \quad \hat{\Delta}_4 = \hat{\Delta}_{\mathbf{k}}^{+-}. \quad (\text{E7})$$

Substituting the above results into Eq. (D13) and setting $\omega = 0$, we obtain the effective Hamiltonian describing superconducting spectral properties of energy bands with predominant aluminum orbital character in the normal state at the Fermi energy,

$$\hat{H}_{\mathbf{k},\text{eff}}^{++} = \begin{pmatrix} \hat{N}_{\mathbf{k},\text{eff}}^{++} + \hat{\xi}_1 & \hat{\Delta}_{\mathbf{k},\text{eff}}^{++} \\ [\hat{\Delta}_{\mathbf{k},\text{eff}}^{++}]^\dagger & -\hat{N}_{-\mathbf{k}}^{++} + \hat{\xi}_2 \end{pmatrix}, \quad (\text{E8})$$

where the energy shifts, arising from the interorbital pairing, are

$$\hat{\xi}_1 = +\hat{\Delta}_{\mathbf{k}}^{+-} \frac{1}{\hat{N}_{-\mathbf{k}}^-} [\hat{\Delta}_{\mathbf{k}}^{+-}]^\dagger, \quad (\text{E9})$$

$$\hat{\xi}_2 = -[\hat{\Delta}_{\mathbf{k}}^{+-}]^\dagger \frac{1}{\hat{N}_{\mathbf{k}}^-} \hat{\Delta}_{\mathbf{k}}^{+-}. \quad (\text{E10})$$

The effective low-energy pairing potential for the predominant aluminum bands takes the form

$$\hat{\Delta}_{\mathbf{k},\text{eff}}^{++} = \hat{\Delta}_{\mathbf{k}}^{++} + \hat{\Delta}_{\mathbf{k}}^{+-} \frac{1}{\hat{N}_{-\mathbf{k}}^-} [\hat{\Delta}_{\mathbf{k}}^{--}]^\dagger \frac{1}{-\hat{N}_{\mathbf{k}}^-} \hat{\Delta}_{\mathbf{k}}^{+-}. \quad (\text{E11})$$

Note that the second term is arising from the interplay between interorbital pairing with pairing of energy bands with predominant Au character.

2. Band basis label with $\nu = \nu' = -$

The effective superconducting Hamiltonian for the predominant Au sector can be derived through a unitary transformation $\hat{\mathcal{H}}_{\mathbf{k}}'' = \hat{U}'^\dagger \hat{\mathcal{H}}_{\mathbf{k}}' \hat{U}'$ with

$$\hat{\mathcal{H}}_{\mathbf{k}}'' = \begin{pmatrix} \hat{N}_{\mathbf{k}}^{--} & \hat{\Delta}_{\mathbf{k}}^{--} & 0 & \hat{\Delta}_{\mathbf{k}}^{+-} \\ [\hat{\Delta}_{\mathbf{k}}^{--}]^\dagger & -\hat{N}_{-\mathbf{k}}^{--} & [\hat{\Delta}_{\mathbf{k}}^{+-}]^\dagger & 0 \\ 0 & \hat{\Delta}_{\mathbf{k}}^{+-} & \hat{N}_{\mathbf{k}}^{++} & \hat{\Delta}_{\mathbf{k}}^{++} \\ [\hat{\Delta}_{\mathbf{k}}^{+-}]^\dagger & 0 & [\hat{\Delta}_{\mathbf{k}}^{++}]^\dagger & -\hat{N}_{-\mathbf{k}}^{++} \end{pmatrix}, \quad (\text{E12})$$

where \hat{U}' is given by

$$(\hat{U}')^{-1} = (\hat{U}')^\dagger = \begin{pmatrix} 0 & 1 & 0 & 0 \\ 0 & 0 & 0 & 1 \\ 1 & 0 & 0 & 0 \\ 0 & 0 & 1 & 0 \end{pmatrix}. \quad (\text{E13})$$

Comparing Eq. (E12) with Eq. (D3), we obtain

$$\hat{N}_1 = \hat{N}_{\mathbf{k}}^{--}, \quad \hat{h}_2 = -\hat{N}_{-\mathbf{k}}^-, \quad (\text{E14})$$

$$\hat{N}_2 = \hat{N}_{\mathbf{k}}^{++}, \quad \hat{h}_1 = -\hat{N}_{-\mathbf{k}}^+, \quad (\text{E15})$$

$$\hat{\Delta}_1 = \hat{\Delta}_{\mathbf{k}}^{+-}, \quad \hat{\Delta}_2 = \hat{\Delta}_{\mathbf{k}}^{--}, \quad (\text{E16})$$

$$\hat{\Delta}_3 = \hat{\Delta}_{\mathbf{k}}^{++}, \quad \hat{\Delta}_4 = \hat{\Delta}_{\mathbf{k}}^{+-}. \quad (\text{E17})$$

At the Fermi energy $\omega = 0$, inserting the above relations to Eq. (D13), we explicitly derive the effective superconducting Hamiltonian for the energy bands with predominant Au orbital character in the normal state for small momenta given by

$$\hat{H}_{\mathbf{k},\text{eff}}^{--} = \begin{pmatrix} \hat{N}_{\mathbf{k}}^{--} + \hat{\xi}_1 & \hat{\Delta}_{\mathbf{k},\text{eff}}^{--} \\ [\hat{\Delta}_{\mathbf{k},\text{eff}}^{--}]^\dagger & -\hat{N}_{-\mathbf{k}}^{--} + \hat{\xi}_2 \end{pmatrix}, \quad (\text{E18})$$

where the energy shifts induced by multiband effects are

$$\hat{\xi}_1 = +\hat{\Delta}_{\mathbf{k}}^{+-} \frac{1}{\hat{N}_{-\mathbf{k}}^{++}} [\hat{\Delta}_{\mathbf{k}}^{+-}]^\dagger, \quad (\text{E19})$$

$$\hat{\xi}_2 = -[\hat{\Delta}_{\mathbf{k}}^{+-}]^\dagger \frac{1}{\hat{N}_{\mathbf{k}}^{++}} \hat{\Delta}_{\mathbf{k}}^{+-}. \quad (\text{E20})$$

Moreover, the effective low-energy pairing potential for the predominant Au bands in the normal state becomes

$$\hat{\Delta}_{\mathbf{k},\text{eff}}^{--} = \hat{\Delta}_{\mathbf{k}}^{--} + \hat{\Delta}_{\mathbf{k}}^{+-} \frac{1}{\hat{N}_{-\mathbf{k}}^{++}} [\hat{\Delta}_{\mathbf{k}}^{++}]^\dagger \frac{1}{-\hat{N}_{\mathbf{k}}^{++}} \hat{\Delta}_{\mathbf{k}}^{+-}. \quad (\text{E21})$$

3. Interorbital sector

To obtain an effective interorbital superconducting Hamiltonian and study the BdG spectra at finite excitation energies, it is helpful to represent the BdG Hamiltonian in the interband basis. This can be done by the unitary transformation $\hat{\mathcal{H}}_{\mathbf{k}}''' = \hat{U}''^\dagger \hat{\mathcal{H}}_{\mathbf{k}}'' \hat{U}''$ with

$$\hat{\mathcal{H}}_{\mathbf{k}}''' = \begin{pmatrix} \hat{N}_{\mathbf{k}}^{++} & \hat{\Delta}_{\mathbf{k}}^{+-} & 0 & \hat{\Delta}_{\mathbf{k}}^{++} \\ [\hat{\Delta}_{\mathbf{k}}^{+-}]^\dagger & -\hat{N}_{-\mathbf{k}}^{--} & [\hat{\Delta}_{\mathbf{k}}^{--}]^\dagger & 0 \\ 0 & \hat{\Delta}_{\mathbf{k}}^{--} & \hat{N}_{\mathbf{k}}^{--} & \hat{\Delta}_{\mathbf{k}}^{+-} \\ [\hat{\Delta}_{\mathbf{k}}^{++}]^\dagger & 0 & [\hat{\Delta}_{\mathbf{k}}^{+-}]^\dagger & -\hat{N}_{-\mathbf{k}}^{++} \end{pmatrix}, \quad (\text{E22})$$

where the unitary matrix \hat{U}'' is given by

$$(\hat{U}'')^{-1} = (\hat{U}'')^\dagger = \begin{pmatrix} 1 & 0 & 0 & 0 \\ 0 & 0 & 1 & 0 \\ 0 & 0 & 0 & 1 \\ 0 & 1 & 0 & 0 \end{pmatrix}. \quad (\text{E23})$$

In this case, comparing Eq. (E22) with Eq. (D3), we arrive at

$$\hat{N}_1 = \hat{N}_{\mathbf{k}}^{++}, \quad \hat{h}_2 = -\hat{N}_{-\mathbf{k}}^-, \quad (\text{E24})$$

$$\hat{N}_2 = \hat{N}_{\mathbf{k}}^{--}, \quad \hat{h}_1 = -\hat{N}_{-\mathbf{k}}^+, \quad (\text{E25})$$

$$\hat{\Delta}_1 = \hat{\Delta}_{\mathbf{k}}^{++}, \quad \hat{\Delta}_2 = \hat{\Delta}_{\mathbf{k}}^{+-}, \quad (\text{E26})$$

$$\hat{\Delta}_3 = \hat{\Delta}_{\mathbf{k}}^{+-}, \quad \hat{\Delta}_4 = \hat{\Delta}_{\mathbf{k}}^{--}. \quad (\text{E27})$$

Since the interorbital pairing happens at finite excitation energy, ω is no longer vanishing and becomes finite. Substituting the above relations into Eq. (D13), we find an explicit form for the effective interorbital superconducting Hamiltonian,

$$\hat{H}_{\mathbf{k},\text{eff}}^{\text{IO}} = \begin{pmatrix} \hat{N}_{\mathbf{k}}^{++} + \hat{\xi}_1 & \hat{\Delta}_{\mathbf{k},\text{eff}}^{+-} \\ [\hat{\Delta}_{\mathbf{k},\text{eff}}^{+-}]^\dagger & -\hat{N}_{-\mathbf{k}}^{--} + \hat{\xi}_2 \end{pmatrix}, \quad (\text{E28})$$

where the energy shifts, induced by the intraband effects, are given by

$$\hat{\xi}_1 = \hat{\Delta}_{\mathbf{k}}^{++} \frac{1}{\omega \hat{\sigma}_0 + \hat{N}_{-\mathbf{k}}^{++}} [\hat{\Delta}_{\mathbf{k}}^{++}]^\dagger, \quad (\text{E29})$$

$$\hat{\xi}_2 = [\hat{\Delta}_{\mathbf{k}}^{--}]^\dagger \frac{1}{\omega \hat{\sigma}_0 - \hat{N}_{\mathbf{k}}^{--}} \hat{\Delta}_{\mathbf{k}}^{--}. \quad (\text{E30})$$

Note that $\hat{H}_{\mathbf{k},\text{eff}}^{\text{IO}}$ breaks particle-hole symmetry due to the different diagonal entries arising from two different energy bands. Finally, the effective 2×2 finite-energy pairing matrix

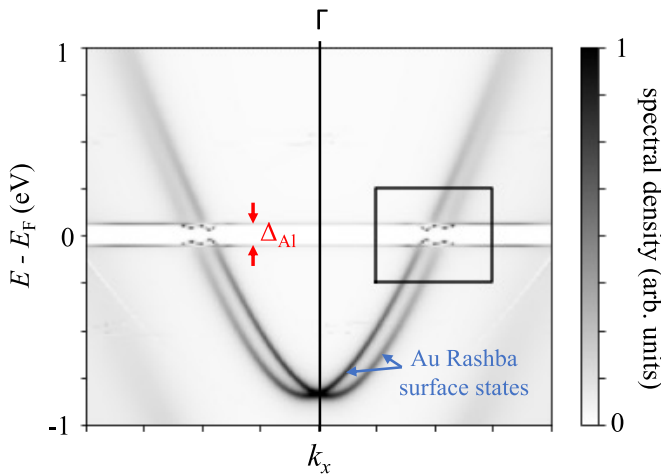


FIG. 9. Superconducting electronic structure of six layers of Au on top of semi-infinite Al. The gray background (i.e., with nonzero spectral density) in most parts of the Brillouin zone reflects the continuum of states in the semi-infinite Al. The spectrum clearly shows the superconducting gap of Al (labeled Δ_{Al}) and the proximity-induced gap in the Au Rashba surface state (marked by the black box). In contrast to the thin-film limit, the finite-energy pairing disappears in the semi-infinite limit as no discrete Al quantum-well states are present.

becomes

$$\hat{\Delta}_{\mathbf{k},\text{eff}}^{\text{IO}} = \hat{\Delta}_{\mathbf{k}}^{+-} + \hat{\Delta}_{\mathbf{k}}^{++} \frac{1}{\omega \hat{\sigma}_0 + \hat{N}_{-\mathbf{k}}^{++}} [\hat{\Delta}_{\mathbf{k}}^{-+}]^\dagger \frac{1}{\hat{\sigma}_0 \omega - \hat{N}_{\mathbf{k}}^{--}} \hat{\Delta}_{\mathbf{k}}^{--}. \quad (\text{E31})$$

Note that the second term originates from the interplay between low-energy bands and their corresponding pairings with finite energy pairing.

APPENDIX F: IMPORTANCE OF THE THIN-FILM LIMIT FOR FINITE-ENERGY PAIRING

In our work, we consider the thin film limit of Al, (i) due to the increased superconducting gap in Al thin films compared to bulk Al, and (ii) because having discrete quantum-well states enables finite-energy pairing. With varying thickness of the Al superconductor, the quantum-well states appear in different locations of the Brillouin zone, which in turn affects the strength of the hybridization of the Al and Au derived states. With increasing thickness, more and more quantum-well states appear and a continuum of states emerges in the semi-infinite limit. In this limit, there is no discrete location in the dispersion where a sharp band of Al intersects with the discrete dispersion of the Rashba surface state of Au. This suppresses the signatures of finite-energy pairing, and the avoided crossings at finite energies are washed out. This can be seen in Fig. 9.

- [1] A. Manchon, H. C. Koo, J. Nitta, S. M. Frolov, and R. A. Duine, New perspectives for Rashba spin-orbit coupling, *Nat. Mater.* **14**, 871 (2015).
- [2] G. Bihlmayer, P. Noël, D. V. Vyalikh, E. V. Chulkov, and A. Manchon, Rashba-like physics in condensed matter, *Nat. Rev. Phys.* **4**, 642 (2022).
- [3] A. Fert, N. Reyren, and V. Cros, Magnetic skyrmions: Advances in physics and potential applications, *Nat. Rev. Mater.* **2**, 17031 (2017).
- [4] M. Z. Hasan and C. L. Kane, Colloquium: Topological insulators, *Rev. Mod. Phys.* **82**, 3045 (2010).
- [5] J. Alicea, Y. Oreg, G. Refael, F. von Oppen, and M. P. A. Fisher, Non-Abelian statistics and topological quantum information processing in 1D wire networks, *Nat. Phys.* **7**, 412 (2011).
- [6] R. M. Lutchyn, E. P. A. M. Bakkers, L. P. Kouwenhoven, P. Krogstrup, C. M. Marcus, and Y. Oreg, Majorana zero modes in superconductor-semiconductor heterostructures, *Nat. Rev. Mater.* **3**, 52 (2018).
- [7] S. M. Frolov, M. J. Manfra, and J. D. Sau, Topological superconductivity in hybrid devices, *Nat. Phys.* **16**, 718 (2020).
- [8] K. Flensberg, F. von Oppen, and A. Stern, Engineered platforms for topological superconductivity and Majorana zero modes, *Nat. Rev. Mater.* **6**, 944 (2021).
- [9] E. I. Rashba, Properties of semiconductors with an extremum loop, *Sov. Phys. Solid State* **2**, 1109 (1960).
- [10] A. Avsar, J. Y. Tan, T. Taychatanapat, J. Balakrishnan, G. K. W. Koon, Y. Yeo, J. Lahiri, A. Carvalho, A. S. Rodin, E. C. T. O'Farrell, A. H. Castro Neto, G. Eda, and B. Özyilmaz, Spin-orbit proximity effect in graphene, *Nat. Commun.* **5**, 4875 (2014).
- [11] M. Gmitra and J. Fabian, Proximity effects in bilayer graphene on monolayer WSe₂: Field-effect spin valley locking, spin-orbit valve, and spin transistor, *Phys. Rev. Lett.* **119**, 146401 (2017).
- [12] J. O. Island, X. Cui, C. Lewandowski, J. Y. Khoo, S. E. M., H. Zhou, D. Rhodes, J. C. Hone, T. Taniguchi, K. Watanabe, L. S. Levitov, M. P. Zaletel, and A. F. Young, Spin-orbit-driven band inversion in bilayer graphene by the van der Waals proximity effect, *Nature (London)* **571**, 85 (2019).
- [13] C. Nayak, S. H. Simon, A. Stern, M. Freedman, and S. Das Sarma, Non-abelian anyons and topological quantum computation, *Rev. Mod. Phys.* **80**, 1083 (2008).
- [14] P. Wei, S. Manna, M. Eich, P. Lee, and J. Moodera, Superconductivity in the surface state of noble metal gold and its fermi level tuning by EuS dielectric, *Phys. Rev. Lett.* **122**, 247002 (2019).
- [15] Y.-M. Xie, K. T. Law, and P. A. Lee, Topological superconductivity in EuS/Au/superconductor heterostructures, *Phys. Rev. Res.* **3**, 043086 (2021).
- [16] P. G. De Gennes, *Superconductivity of Metals and Alloys* (Benjamin, New York, 1966).
- [17] J.-X. Zhu, *Bogoliubov-de Gennes Method and Its Applications* (Springer International, Switzerland, 2016).
- [18] L. N. Oliveira, E. K. U. Gross, and W. Kohn, Density-functional theory for superconductors, *Phys. Rev. Lett.* **60**, 2430 (1988).
- [19] M. Lüders, M. A. L. Marques, N. N. Lathiotakis, A. Floris, G. Profeta, L. Fast, A. Continenza, S. Massidda, and E. K. U. Gross, Ab initio theory of superconductivity. I. Density functional formalism and approximate functionals, *Phys. Rev. B* **72**, 024545 (2005).

- [20] G. Csire, B. Újfalussy, J. Cserti, and B. Győrfy, Multiple scattering theory for superconducting heterostructures, *Phys. Rev. B* **91**, 165142 (2015).
- [21] M. Kawamura, Y. Hizume, and T. Ozaki, Benchmark of density functional theory for superconductors in elemental materials, *Phys. Rev. B* **101**, 134511 (2020).
- [22] A. Linscheid, A. Sanna, F. Essenberg, and E. K. U. Gross, Ab initio theory of superconductivity in a magnetic field. I. Spin density functional theory for superconductors and Eliashberg equations, *Phys. Rev. B* **92**, 024505 (2015).
- [23] M. S. Scheurer, D. F. Agterberg, and J. Schmalian, Selection rules for Cooper pairing in two-dimensional interfaces and sheets, *npj Quantum Mater.* **2**, 9 (2017).
- [24] S. LaShell, B. A. McDougall, and E. Jensen, Spin splitting of an Au(111) surface state band observed with angle resolved photoelectron spectroscopy, *Phys. Rev. Lett.* **77**, 3419 (1996).
- [25] A. Varykhalov, D. Marchenko, M. R. Scholz, E. D. L. Rienks, T. K. Kim, G. Bihlmayer, J. Sánchez-Barriga, and O. Rader, Ir(111) surface state with giant Rashba splitting persists under graphene in air, *Phys. Rev. Lett.* **108**, 066804 (2012).
- [26] C. R. Ast, J. Henk, A. Ernst, L. Moreschini, M. C. Falub, D. Pacilé, P. Bruno, K. Kern, and M. Grioni, Giant spin splitting through surface alloying, *Phys. Rev. Lett.* **98**, 186807 (2007).
- [27] S. Nadj-Perge, S. M. Frolov, E. P. A. M. Bakkers, and L. P. Kouwenhoven, Spin-orbit qubit in a semiconductor nanowire, *Nature (London)* **468**, 1084 (2010).
- [28] P. D. C. King, R. C. Hatch, M. Bianchi, R. Ovsyannikov, C. Lupulescu, G. Landolt, B. Slomski, J. H. Dil, D. Guan, J. L. Mi, E. D. L. Rienks, J. Fink, A. Lindblad, S. Svensson, S. Bao, G. Balakrishnan, B. B. Iversen, J. Osterwalder, W. Eberhardt, F. Baumberger *et al.*, Large tunable Rashba spin splitting of a two-dimensional electron gas in Bi₂Se₃, *Phys. Rev. Lett.* **107**, 096802 (2011).
- [29] D. Breunig, S.-B. Zhang, B. Trauzettel, and T. M. Klapwijk, Directional electron filtering at a superconductor-semiconductor interface, *Phys. Rev. B* **103**, 165414 (2021).
- [30] F. Ando, Y. Miyasaka, T. Li, J. Ishizuka, T. Arakawa, Y. Shiota, T. Moriyama, Y. Yanase, and T. Ono, Observation of superconducting diode effect, *Nature (London)* **584**, 373 (2020).
- [31] H. Wu, Y. Wang, Y. Xu, P. K. Sivakumar, C. Pasco, U. Filippozzi, S. S. P. Parkin, Y.-J. Zeng, T. McQueen, and M. N. Ali, The field-free Josephson diode in a van der Waals heterostructure, *Nature (London)* **604**, 653 (2022).
- [32] Y. Zhang, Y. Gu, P. Li, J. Hu, and K. Jiang, General theory of Josephson diodes, *Phys. Rev. X* **12**, 041013 (2022).
- [33] A. Banerjee, A. Sundaresh, R. Ganesan, and P. S. A. Kumar, Signatures of topological superconductivity in bulk-insulating topological insulator BiSbTe_{1.25}Se_{1.75} in proximity with superconducting NbSe₂, *ACS Nano* **12**, 12665 (2018).
- [34] J. Linder and A. V. Balatsky, Odd-frequency superconductivity, *Rev. Mod. Phys.* **91**, 045005 (2019).
- [35] G. Tang, C. Bruder, and W. Belzig, Magnetic field-induced “mirage” gap in an Ising superconductor, *Phys. Rev. Lett.* **126**, 237001 (2021).
- [36] M. Bahari, S.-B. Zhang, and B. Trauzettel, Intrinsic finite-energy Cooper pairing in $j = 3/2$ superconductors, *Phys. Rev. Res.* **4**, L012017 (2022).
- [37] M. Bahari, S.-B. Zhang, C.-A. Li, S.-J. Choi, C. Timm, and B. Trauzettel, New type of helical topological superconducting pairing at finite excitation energies, [arXiv:2210.11955](https://arxiv.org/abs/2210.11955) [cond-mat.mes-hall].
- [38] A. Moreo, M. Daghofer, A. Nicholson, and E. Dagotto, Interband pairing in multiorbital systems, *Phys. Rev. B* **80**, 104507 (2009).
- [39] L. Komendová, A. V. Balatsky, and A. M. Black-Schaffer, Experimentally observable signatures of odd-frequency pairing in multiband superconductors, *Phys. Rev. B* **92**, 094517 (2015).
- [40] C. Triola and A. V. Balatsky, Pair symmetry conversion in driven multiband superconductors, *Phys. Rev. B* **95**, 224518 (2017).
- [41] D. Chakraborty and A. M. Black-Schaffer, Interplay of finite-energy and finite-momentum superconducting pairing, *Phys. Rev. B* **106**, 024511 (2022).
- [42] G. Nicolay, F. Reinert, S. Hübner, and P. Blaha, Spin-orbit splitting of the L-gap surface state on Au(111) and Ag(111), *Phys. Rev. B* **65**, 033407 (2001).
- [43] J. Henk, A. Ernst, and P. Bruno, Spin polarization of the L-gap surface states on Au(111), *Phys. Rev. B* **68**, 165416 (2003).
- [44] J. Henk, M. Hoesch, J. Osterwalder, A. Ernst, and P. Bruno, Spin-orbit coupling in the L-gap surface states of Au(111): spin-resolved photoemission experiments and first-principles calculations, *J. Phys.: Condens. Matter* **16**, 7581 (2004).
- [45] M. Hoesch, M. Muntwiler, V. N. Petrov, M. Hengsberger, L. Pattthey, M. Shi, M. Falub, T. Greber, and J. Osterwalder, Spin structure of the Shockley surface state on Au(111), *Phys. Rev. B* **69**, 241401(R) (2004).
- [46] S. N. P. Wissing, C. Eibl, A. Zumbülte, A. B. Schmidt, J. Braun, J. Minár, H. Ebert, and M. Donath, Rashba-type spin splitting at Au(111) beyond the Fermi level: The other part of the story, *New J. Phys.* **15**, 105001 (2013).
- [47] *Al Crystal Structure: Datasheet from “PAULING FILE Multinaries Edition – 2022” in SpringerMaterials*, edited by P. Villars and K. Cenzual (Springer-Verlag, Berlin, 2016).
- [48] *Au Crystal Structure: Datasheet from “PAULING FILE Multinaries Edition – 2022” in SpringerMaterials*, edited by P. Villars and K. Cenzual (Springer-Verlag, Berlin, 2016).
- [49] The JuKKR developers, The Jülich KKR Codes (2022), <https://jukkr.fz-juelich.de>.
- [50] P. Rübmann and S. Blügel, Density functional Bogoliubov-de Gennes analysis of superconducting Nb and Nb(110) surfaces, *Phys. Rev. B* **105**, 125143 (2022).
- [51] S. Vajna, E. Simon, A. Szilva, K. Palotas, B. Újfalussy, and L. Szunyogh, Higher-order contributions to the Rashba-Bychkov effect with application to the Bi/Ag(111) surface alloy, *Phys. Rev. B* **85**, 075404 (2012).
- [52] J. Bardeen, L. N. Cooper, and J. R. Schrieffer, Theory of superconductivity, *Phys. Rev.* **108**, 1175 (1957).
- [53] M. B. Suvasini, W. M. Temmerman, and B. L. Győrfy, Computational aspects of density-functional theories of superconductors, *Phys. Rev. B* **48**, 1202 (1993).
- [54] G. Csire, S. Schönecker, and B. Újfalussy, First-principles approach to thin superconducting slabs and heterostructures, *Phys. Rev. B* **94**, 140502(R) (2016).
- [55] T. G. Saunderson, J. F. Annett, B. Újfalussy, G. Csire, and M. Gradhand, Gap anisotropy in multiband superconductors based on multiple scattering theory, *Phys. Rev. B* **101**, 064510 (2020).

- [56] G. Csire, J. Cserti, I. Túttó, and Balázs Újfalussy, Prediction of superconducting transition temperatures of heterostructures based on the quasiparticle spectrum, *Phys. Rev. B* **94**, 104511 (2016).
- [57] G. Csire, J. Cserti, and B. Újfalussy, First principles based proximity effect of superconductor–normal metal heterostructures, *J. Phys.: Condens. Matter* **28**, 495701 (2016).
- [58] P. Rüßmann and S. Blügel, Proximity induced superconductivity in a topological insulator, [arXiv:2208.14289](https://arxiv.org/abs/2208.14289).
- [59] T. G. Saunders, Z. Gyorgypal, J. F. Annett, G. Csire, B. Újfalussy, and M. Gradhand, Real-space multiple scattering theory for superconductors with impurities, *Phys. Rev. B* **102**, 245106 (2020).
- [60] B. Nyári, A. Lászlóffy, L. Szunyogh, G. Csire, K. Park, and B. Újfalussy, Relativistic first-principles theory of Yu-Shiba-Rusinov states applied to Mn adatoms and Mn dimers on Nb(110), *Phys. Rev. B* **104**, 235426 (2021).
- [61] Note that both pseudo-spin-singlet and triplet components are purely imaginary due to the arbitrary choice of a complex phase.
- [62] J. Eisenstein, Superconducting elements, *Rev. Mod. Phys.* **26**, 277 (1954).
- [63] R. Meservey and P. M. Tedrow, Properties of very thin aluminium films, *J. Appl. Phys.* **42**, 51 (1971).
- [64] N. A. Court, A. J. Ferguson, and R. G. Clark, Energy gap measurement of nanostructures aluminium thin films for single Cooper-pair devices, *Supercond. Sci. Technol.* **21**, 015013 (2008).
- [65] W. M. J. van Weerdenburg, A. Kamlapure, E. H. Fyhn, X. Huang, N. P. E. van Mullekom, M. Steinbrecher, P. Krogstrup, J. Linder, and A. A. Khajetoorians, Extreme enhancement of superconductivity in epitaxial aluminum near the monolayer limit, *Sci. Adv.* **9**, eadf5500 (2023).
- [66] J. Schwenk, S. Kim, J. Berwanger, F. Ghahari, D. Walkup, M. R. Slot, S. T. Le, W. G. Cullen, S. R. Blankenship, S. Vranjkovic, H. J. Hug, Y. Kuk, F. J. Giessibl, and J. A. Stroscio, Achieving μeV tunneling resolution in an in-operando scanning tunneling microscopy, atomic force microscopy, and magnetotransport system for quantum materials research, *Rev. Sci. Instrum.* **91**, 071101 (2020).
- [67] K. Ishizaka, M. S. Bahramy, H. Murakawa, M. Sakano, T. Shimojima, T. Sonobe, K. Koizumi, S. Shin, H. Miyahara, A. Kimura, K. Miyamoto, T. Okuda, H. Namatame, M. Taniguchi, R. Arita, N. Nagaosa, K. Kobayashi, Y. Murakami, R. Kumai, Y. Kaneko *et al.*, Giant Rashba-type spin splitting in bulk BiTeI, *Nat. Mater.* **10**, 521 (2011).
- [68] Z. Liu, S. Thirupathiah, A. N. Yaresko, S. Kushwaha, Q. Gibson, W. Xia, Y. Guo, D. Shen, R. J. Cava, and S. V. Borisenko, A giant bulk-type Dresselhaus splitting with 3D chiral spin texture in IrBiSe, *Phys. Status Solidi RRL* **14**, 1900684 (2020).
- [69] M. Aghaee *et al.* (Microsoft Quantum), InAs-Al hybrid devices passing the topological gap protocol, *Phys. Rev. B* **107**, 245423 (2023).
- [70] A. Geim and I. Grigorieva, Van der Waals heterostructures, *Nature (London)* **499**, 419 (2013).
- [71] E. Y. Andrei, D. K. Efetov, P. Jarillo-Herrero, A. H. MacDonald, K. F. Mak, T. Senthil, E. Tutuc, A. Yazdani, and A. F. Young, The marvels of moiré materials, *Nat. Rev. Mater.* **6**, 201 (2021).
- [72] C. Triola, J. Cayao, and A. M. Black-Schaffer, The role of odd-frequency pairing in multiband superconductors, *Ann. Phys.* **532**, 1900298 (2020).
- [73] M. Eschrig, Spin-polarized supercurrents for spintronics, *Phys. Today* **64**, 43 (2011).
- [74] J. Linder and J. Robinson, Superconducting spintronics, *Nat. Phys.* **11**, 307 (2015).
- [75] H. Kim, K. Wang, Y. Nakajima, R. Hu, S. Ziemak, P. Syers, L. Wang, H. Hodovanets, J. D. Denlinger, P. M. R. Brydon, D. F. Agterberg, M. A. Tanatar, R. Prozorov, and J. Paglione, Beyond triplet: Unconventional superconductivity in a spin-3/2 topological semimetal, *Sci. Adv.* **4**, eaao4513 (2018).
- [76] S. Khim, J. F. Landaeta, J. Banda, N. Bannor, M. Brando, P. M. R. Brydon, D. Hafner, R. Kuchler, R. Cardoso-Gil, U. Stockert, A. P. Mackenzie, D. F. Agterberg, C. Geibel, and E. Hassinger, Field-induced transition within the superconducting state of CeRh₂As₂, *Science* **373**, 1012 (2021).
- [77] H. Ebert, D. Ködderitzsch, and J. Minár, Calculating condensed matter properties using the KKR-Green's function method – recent developments and applications, *Rep. Prog. Phys.* **74**, 096501 (2011).
- [78] J. Zablouil, R. Hammerling, L. Szunyogh, and P. Weinberger, *Electron Scattering in Solid Matter: A Theoretical and Computational Treatise*, Springer Series in Solid-State Sciences Vol. 147 (Springer, New York, 2005).
- [79] S. H. Vosko, L. Wilk, and M. Nusair, Accurate spin-dependent electron liquid correlation energies for local spin density calculations: A critical analysis, *Can. J. Phys.* **58**, 1200 (1980).
- [80] N. Stefanou, H. Akai, and R. Zeller, An efficient numerical method to calculate shape truncation functions for Wigner-Seitz atomic polyhedra, *Comput. Phys. Commun.* **60**, 231 (1990).
- [81] N. Stefanou and R. Zeller, Calculation of shape-truncation functions for Voronoi polyhedra, *J. Phys.: Condens. Matter* **3**, 7599 (1991).
- [82] P. Rüßmann, F. Bertoldo, J. Bröder, J. Wasmer, R. Mozumder, J. Chico, and S. Blügel, JuDFTteam/aiida-kr: AiiDA Plugin for the JuKKR codes, [Zenodo](https://zenodo.org/record/5211111) (2021).
- [83] P. Rüßmann, F. Bertoldo, and S. Blügel, The AiiDA-KKR plugin and its application to high-throughput impurity embedding into a topological insulator, *npj Comput. Mater.* **7**, 13 (2021).
- [84] S. P. Huber, S. Zoupanos, M. Uhrin, L. Talirz, L. Kahle, R. Häuselmann, D. Gresch, T. Müller, A. V. Yakutovich, C. W. Andersen, F. F. Ramirez, C. S. Adorf, F. Gargiulo, S. Kumbhar, E. Passaro, C. Johnston, A. Merkys, A. Cepellotti, N. Mounet, N. Marzari *et al.*, AiiDA 1.0, a scalable computational infrastructure for automated reproducible workflows and data provenance, *Sci. Data* **7**, 300 (2020).
- [85] M. D. Wilkinson, M. Dumontier, I. J. Aalbersberg, G. Appleton, M. Axton, A. Baak, N. Blomberg, J.-W. Boiten, L. B. da Silva Santos, P. E. Bourne, J. Bouwman, A. J. Brookes, T. Clark, M. Crosas, I. Dillo, O. Dumon, S. Edmunds, C. T. Evelo, R. Finkers, A. Gonzalez-Beltran *et al.*, The FAIR Guiding Principles for scientific data management and stewardship, *Sci. Data* **3**, 160018 (2016).

- [86] L. Talirz, S. Kumbhar, E. Passaro, A. V. Yakutovich, V. Granata, F. Gargiulo, M. Borelli, M. Uhrin, S. P. Huber, S. Zoupanos, C. S. Adorf, C. W. Andersen, O. Schütt, C. A. Pignedoli, D. Passerone, J. Van de Vondele, G. P. Thomas C. Schulthess, B. Smit, and N. Marzari, Materials Cloud, a platform for open computational science, *Sci. Data* **7**, 299 (2020).
- [87] P. Rübmann, M. Bahari, S. Blügel, and B. Trauzettel, Dataset of Proximity-induced Cooper pairing at low and finite energies in the gold Rashba surface state, *Materials Cloud Archive* 2023.100 (2023).
- [88] <https://github.com/JuDFTteam/aiida-kkr>; <https://iffgit.fz-juelich.de/kkr/jukkr>.